Computers and Geotechnics 197 (2026) 108273

Contents lists available at ScienceDirect

Computers and Geotechnics

journal homepage: www.elsevier.com/locate/compgeo

Efficient MLM-DRM framework for seismic performance analysis of 3D tunnels in complex geologic media

Bhavesh Banjare [a,*], Gauri Ranjan Krishna Chand Avatar [b], Goudappa Ramanagouda Dodagoudar [a]

[a] Computational Geomechanics Laboratory, Department of Civil Engineering, Indian Institute of Technology Madras, Chennai 600036, Tamil Nadu, India
[b] Department of Aerospace Engineering, Indian Institute of Science, Bengaluru 560012, Karnataka, India

ARTICLE INFO

Keywords:
Tunnel response
Inclined layered media
Asynchronous ground motion
Fault inclination
MLM-DRM
Seismic performance

ABSTRACT

Underground tunnels are critical components of transportation and utility networks worldwide, often serving as seismic lifelines in regions prone to earthquakes. Underground tunnel is usually very long, and passing through complex geologic media having varying stiffness and impedance contract, due to which it possesses complex dynamic characteristics. A spatial variation of earthquake ground motion is an important factor that cannot be ignored in the design and safety evaluation of tunnel structures. A realistic representation of ground-motion effects–such as asynchronous fault rupture and wave-passage phenomena that occur during actual earthquakes is essential for an accurate assessment of seismic performance. This study examines the seismic performance of tunnels, considering three-dimensional effects, embedded in complex, inclined geologic formations subjected to asynchronous ground motions using Multi-Layer Modified Domain Reduction Method (MLM-DRM). The MLM-DRM framework incorporates layer-specific damping, heterogeneous soil properties, and asynchronous wavefield arrival resulting from fault-rupture mechanisms. Various combinations of inclined geologic layers ranging from 5° to 60° and two oblique incident wave loadings (30° and 45°) are modeled to capture wave-passage effects associated with fault rupture. Three tunnel cross-sections–circular, square, and horseshoe, are considered, each sections normalized to have the same opening area for geometric consistency. The von Mises stress distributions around the tunnel circumference reveal that the asynchronous fault rupture and wave-passage effects significantly amplify the stresses, particularly in steeply inclined geologic media. The deformed shapes of the tunnel cross-sections obtained from the MLM-DRM demonstrate the necessity of incorporating asynchronous excitations and inclined stratigraphy in the seismic design and performance assessment of underground structures.

1. Introduction

Underground infrastructures such as transportation tunnels, utility conduits, caverns, and energy corridors are crucial to modern urban systems for various applications worldwide. Their importance becomes pronounced in seismically active regions, where tunnels frequently serve as lifeline facilities during and after earthquakes. Although, the underground structures generally experience reduced seismic demand compared to surface facilities due to confinement effects, they remain vulnerable to complex subsurface conditions, including inclined layered geology, spatial variability of ground motions, asynchronous fault rupture, and near-fault wave phenomena (Sharma and Judd, 1991; Gurung and Iwao, 1998; Yu et al., 2016; Zhang et al., 2018; Wu et al., 2021; Tian et al., 2023; Wu et al., 2024; Banjare and Avatar, 2024; Cui et al., 2025; Veeraraghavan and Banjare, 2025). Past earthquake events such as the 1999 Chi-Chi earthquake (Wang et al., 2001), the 2008 Wenchuan earthquake (Chen et al., 2014; Shen et al., 2014; Yu et al., 2016), the 2016 Kumamoto earthquake (Zhang et al., 2018), the 2022 Menyuan earthquake (Chen et al., 2023; Huang et al., 2024), and the 2023 Turkey-Syria earthquake (Aydan et al., 2024), where tunnels experienced severe deformations, cracking, joint failures, and localized collapse. These events highlight the complexity of tunnel-fault interaction and inadequacy of simplified design assumptions in faulted or inclined geologic formations. Therefore, a systematic assessment of tunnel response, a proper understanding of the governing failure mechanisms, and the development of improved resilience-oriented design

* Corresponding author.
E-mail addresses: ce23d035@smail.iitm.ac.in (B. Banjare), krishnaagr@iisc.ac.in (G.R.K.C. Avatar), goudar@civil.iitm.ac.in (G.R. Dodagoudar).

https://doi.org/10.1016/j.compgeo.2026.108273
Received 6 February 2026; Received in revised form 16 May 2026; Accepted 18 May 2026
0266-352X/© 2026 Elsevier Ltd. All rights are reserved, including those for text and data mining, AI training, and similar technologies.

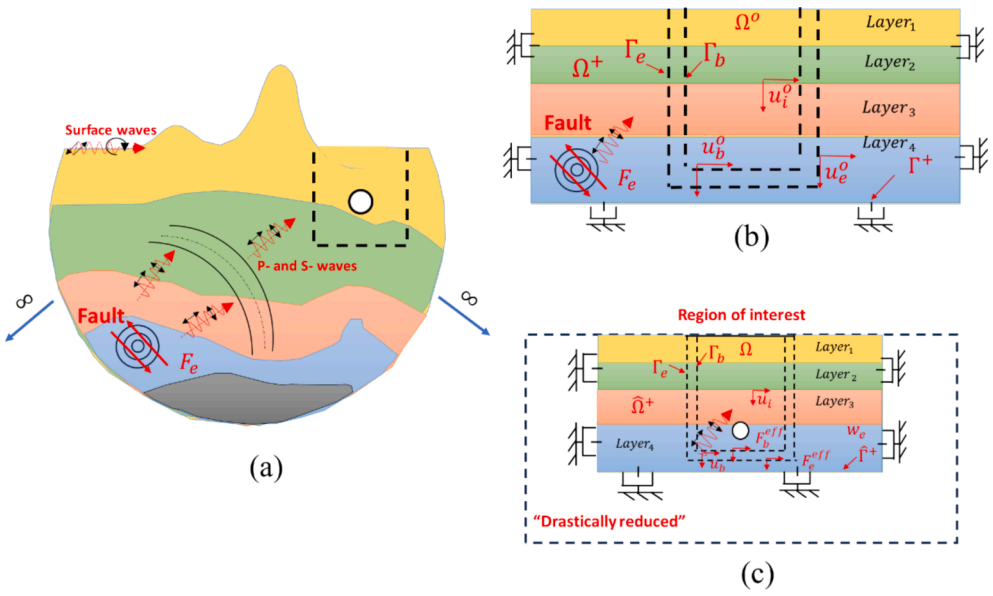


Fig. 1. Schematic of the computational domain (a) Large model considering tunnel, geological features and seismic ground motion (F_e), (b) Free-field analysis considering geological features and F_e, and (c) Reduced model analysis considering tunnel and DRM layer forces [computed in (b)].

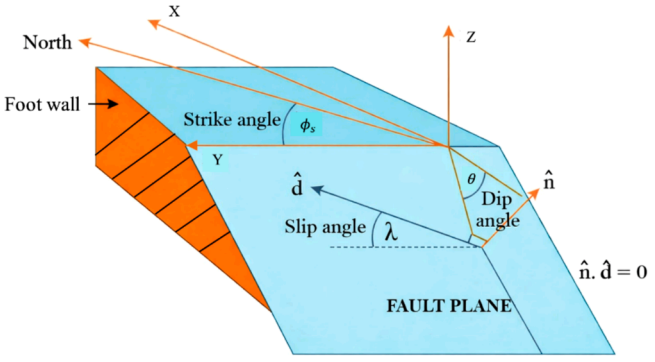


Fig. 2. Fault-plane parameters–Φ_s is the strike, λ is the slip direction, θ is the dip angle, $\hat{d}$ is the slip vector, and $\hat{n}$ is the normal vector in the fault plane (Aki and Richards, 2002).

methodologies are needed to ensure the safety and functionality of lifeline tunnel systems constructed within active fault environments.

Tunnels usually extend over multiple kilometers, traverse various geological units with different material characteristics, and are constructed using the various excavation and support techniques. These attributes make their dynamic behaviour inherently complex and sensitive to spatial changes in ground conditions. Moreover, real earthquakes seldom generate uniform shaking along the tunnel alignment; instead, spatial variability of ground motion, asynchronous fault rupture, and wave-passage effects (Li and Song, 2015; Huang et al., 2017; Fabozzi et al., 2018; Zou et al., 2018) can significantly alter the seismic demand on underground structures. In scenarios involving dipping strata or faulted geological zones, incident seismic waves undergo refraction, mode conversion, amplification, and scattering, producing highly non-uniform, directionally dependent stress distributions on tunnel linings. Traditional analytical approaches often relying on assumptions of homogeneous soil profiles (Lee and Cao, 1989; Lee and Karl, 1992; Lin et al., 2010), vertically propagating waves (Hatzigeorgiou and Beskos, 2010; Wang et al., 2023), or idealized tunnel geometries, hence, they are insufficient to represent these complex wave-soil-structure interaction mechanisms.

Analytical and semi-analytical methods have historically offered

Algorithm MLMDRM Framework for 3D Seismic Analysis of Tunnel Under Asynchronous Ground Motion

Step I: Free-Field Analysis (without tunnel)
- Define soil-fault domain and perform free-field seismic analysis.
- Model seismic excitation using:
  - Seismic moment tensor $M_0(t)$
  - Fault dip angle θ_{dip}
  - Slip and rupture rate, epicenter, rupture velocity
  - Fault dimensions $L \times w$
- Choose spatial Δx and temporal Δt discretization
- Define soil-tunnel interaction region for future use

Compute DRM Forces
- Extract nodal forces F^{drm} at DRM layer boundary from Step I results

Step II: Near-Field Tunnel Analysis
- Construct smaller domain (near-field) including the tunnel
- Apply F^{eff} as boundary input to the DRM layer
- Perform dynamic simulation to obtain tunnel response

Accuracy Verification
- Perform full-domain large model simulation including fault and tunnel
- Compare large model results with DRM-based Step II results

Conclusion

if Step II results ≈ Large model results **then**
  Algorithm is verified
else
  Reassess mesh, time step, or boundary accuracy
end if

Fig. 3. Flowchart of the MLM-DRM Framework for 3D seismic analysis of tunnel.

valuable insights into seismic wave propagation, but their applicability is limited to simplified geometries and homogeneous domains. Classical studies on horizontally polarized shear (SH) wave amplification and idealised topographic effects demonstrate sensitivity to incidence angle, wavelength, and boundary curvature (Trifunac, 1972; Sills, 1978). Boundary integral formulations further enabled modeling of wedges and simple hills (Sánchez-Sesma et al., 1982; Sánchez-Sesma, 1990), while subsequent analytical treatments estimated vibration frequencies of idealised landforms (Paolucci, 2002) and scattering effects around cavities (Smerzini et al., 2009). However, these approaches cannot capture the complexities of real geological settings involving heterogeneous stratigraphy, inclined layers, mode conversion, or surface-wave generation at material interfaces. Additionally, they are inherently incapable of representing asynchronous fault rupture, spatial variability, and oblique wave passage phenomena central to realistic seismic

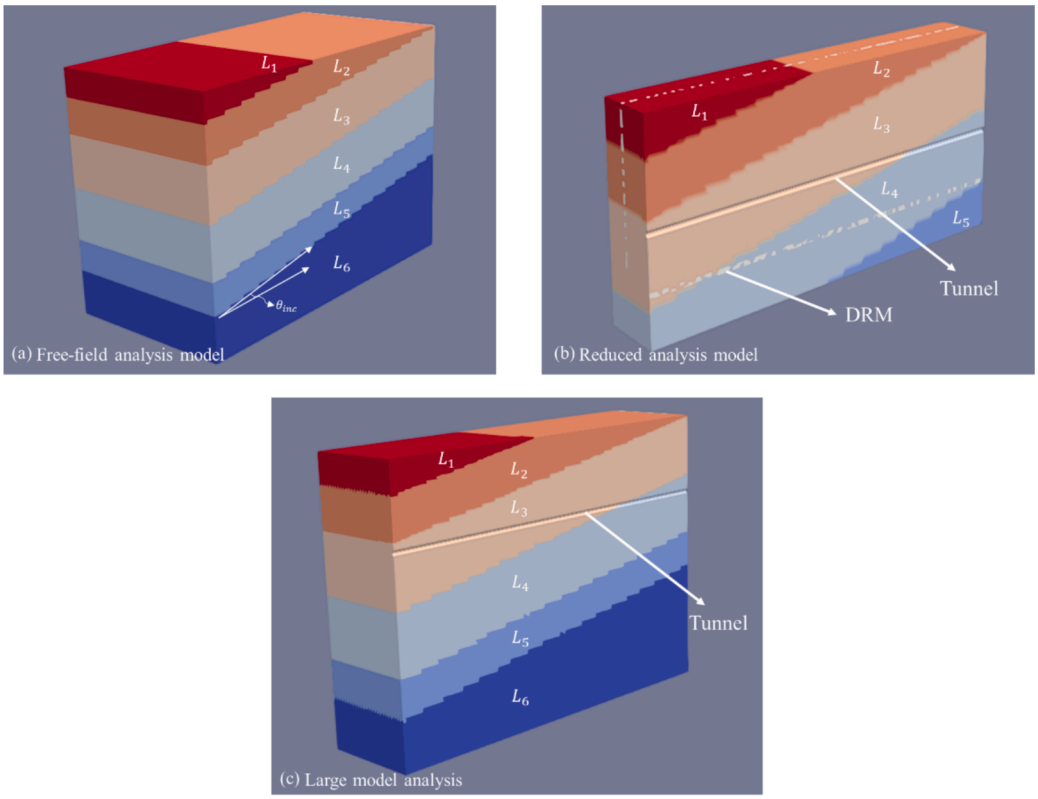


Fig. 4. Problem domain: (a) Free-field model without tunnel, (b) Reduced model with tunnel and DRM layer, and (c) Large model with tunnel (Benchmark problem).

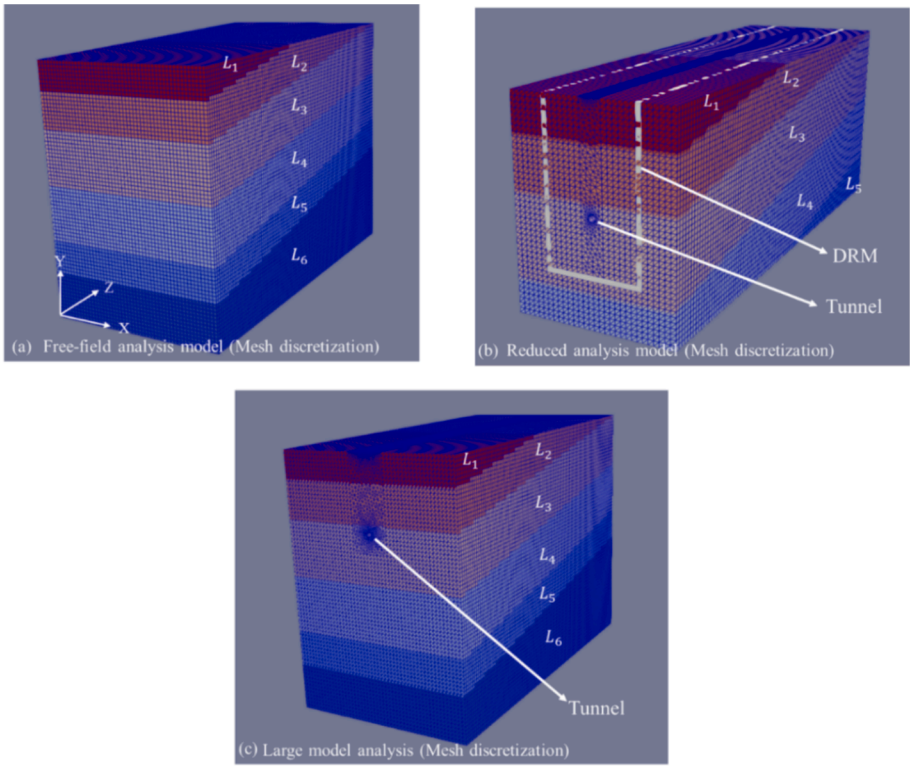


Fig. 5. Finite element discretization of the problem domain: (a) Free-field model without tunnel, (b) Reduced model with tunnel and DRM layer, and (c) Large model with tunnel.

response analysis of tunnels in faulted or inclined stratigraphy.

Finite Difference Method (FDM) has been a mainstay in seismology due to its computational efficiency and ease of implementation for wave propagation studies. Early applications focused on two-dimensional (2D) layered elastic media or mountain-top amplifications (Alterman and Karal, 1968; Boore, 1972). Later work expanded into earthquake-

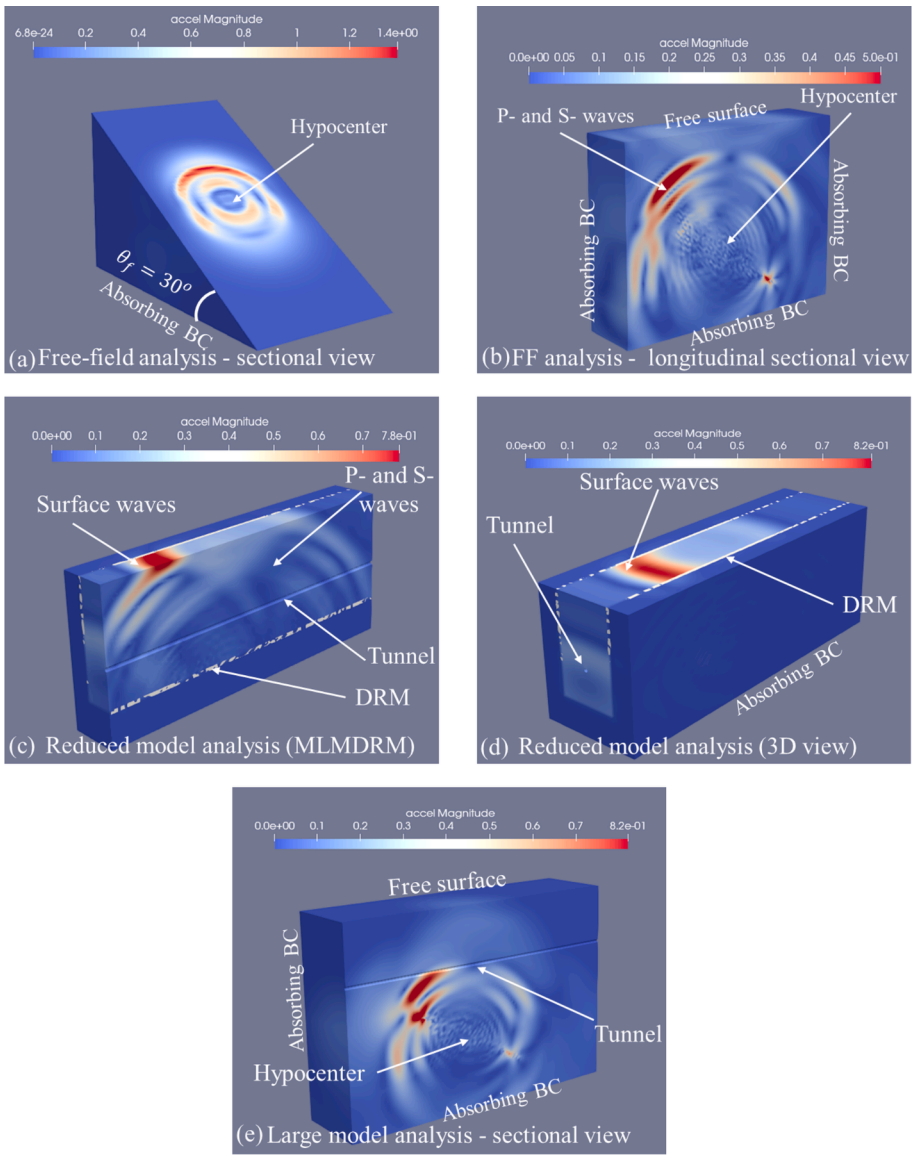


Fig. 6. Schematic of problem domain for MLM-DRM: (a) Free-field simulation with an asynchronously rupturing fault inclined at 30°, (b) Longitudinal section of the free-field model showing DRM layer force evaluation, (c) Reduced-domain analysis of the 3D tunnel subjected to DRM forces, (d) Three-dimensional view of the reduced MLM-DRM model, and (e) Longitudinal section of the large-domain model incorporating asynchronous fault rupture at 30° and the tunnel (Benchmark problem).

specific wavefield simulations, including large-scale SH and Primary-Vertically polarized shear (P-SV) wave propagation analyses (Vidale and Helmberger, 1988; Levander, 2012). Irregular-grid formulations (Opršal and Zahradník, 2012) and octree-based approaches improved adaptability for variable mesh density in finite difference simulations. Nevertheless, structured FDM grids remain limited when modeling irregular tunnel geometries, steeply dipping layered geology, or fault zones. The need to refine grid spacing based on the lowest near-surface wave speed forces fine resolution across the entire domain, substantially increasing computational cost. Moreover, accurately imposing asynchronous wave arrival, non-vertical incidence, and multi-layer impedance contrasts remain difficult within the conventional FDM, restricting its suitability for comprehensive tunnel-fault interaction studies.

Finite Element Method (FEM) provides flexibility for simulating complex tunnel geometries, layered media, and nonlinear material behaviour, making it useful for advanced geotechnical earthquake analysis. The FEM has been successfully applied to heterogeneous basins, strong topographic settings, and intricate soil-structure interaction problems (Bielak and Christiano, 1984; Zienkiewicz et al., 1985; Semblat et al., 2005). However, modeling large three-dimensional (3D) domains at seismic wavelengths requires dense meshes and small-time steps, resulting in high computational cost. Hybrid approaches have therefore emerged, coupling FEM with FDM, boundary element method (BEM), or infinite elements to balance computational cost and modeling accuracy (Moczo et al., 1997; Wuttke et al., 2011). Additional studies have explored hybrid finite element method-infinite element method (FEM-IEM) and scaled boundary finite element method (SBFEM), are the powerful techniques for wave propagation in saturated or layered media (Seo et al., 2007; Heider et al., 2011; Schauer et al., 2011). However, these hybrid frameworks broaden modeling capability, they still struggle with the same extreme deficiencies associated with semi-analytical methods such as strongly inclined stratigraphy, steep geologic interfaces, and asynchronous wave-passage effects, which require precise wavefield control not easily achieved through traditional numerical coupling.

Bielak et al. (2003) have introduced the Domain Reduction Method (DRM) for seismic input modeling by enabling accurate wavefield injection into a reduced computational domain while eliminating

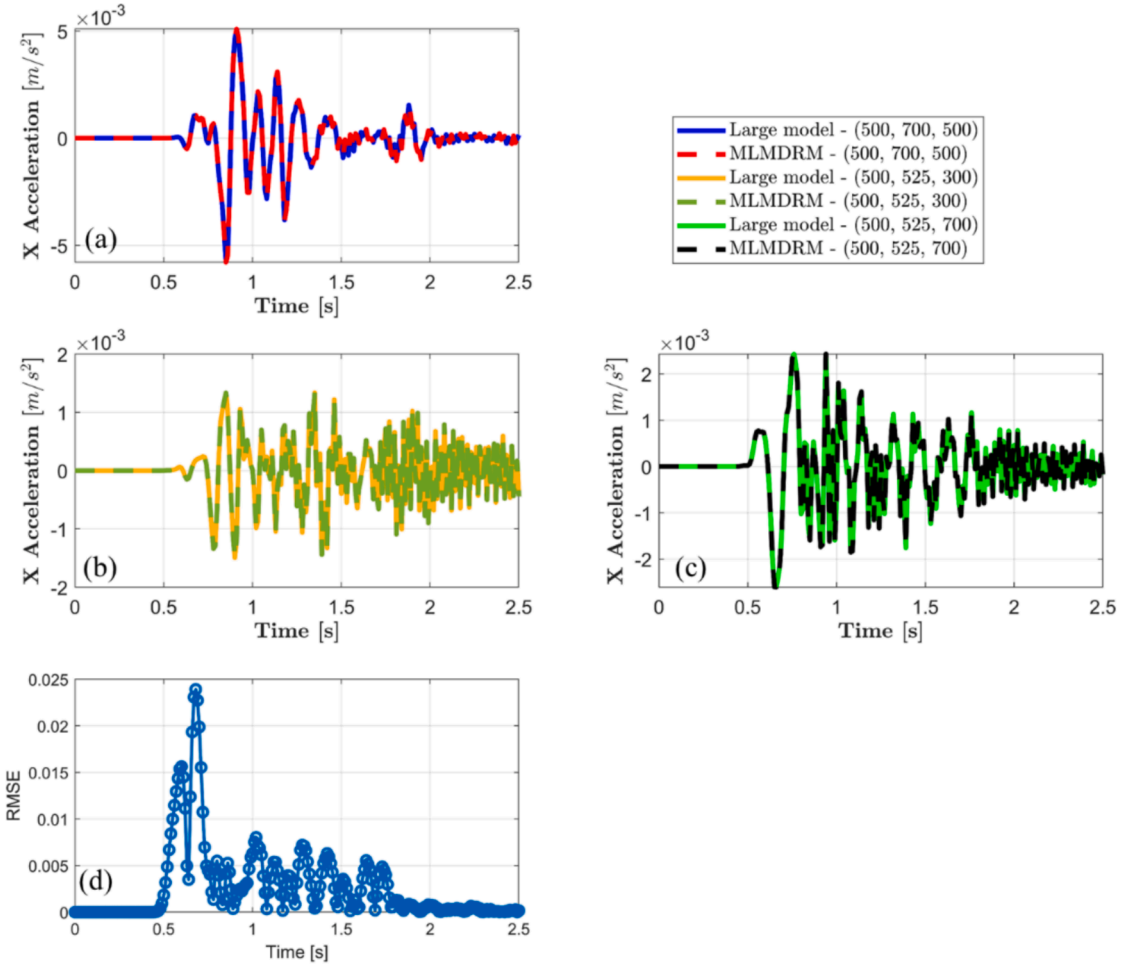


Fig. 7. Comparison of X-direction acceleration component obtained from the large and reduced models (MLM-DRM) at (a) [X = 500 m, Y = 700 m, Z = 500 m], (b) [X = 500 m, Y = 525 m, Z = 300 m], (c) [X = 500 m, Y = 525 m, Z = 700 m], and (d) Root mean square error (RMSE) between the two models.

boundary reflections. The DRM involves two-step procedure: (i) free-field simulation without considering the presence of structure in the problem domain, (ii) equivalent nodal force application, which proves to be an effective approach for soil-structure interaction and basin-scale modeling (Yoshimura et al., 2003; Corigliano et al., 2011; Yuan et al., 2023; Fang et al., 2024). Subsequent extensions to the DRM have enabled consolidation analyses, and realistic modeling of boundary conditions (Kontoe et al., 2008, 2009). However, the classical DRM formulation assumes horizontally layered geology, making it less suitable for inclined, heterogeneous, or fault-intersected geological profiles. Modern tunnel engineering increasingly requires modeling asynchronous ground motions, wave-passage effects, and finite-fault rupture simulation, all of which generate spatially varying input motions that cannot be represented through vertically propagating or uniform boundary motions (Anastasopoulos et al., 2007; Huang et al., 2017; Zhong et al., 2020). These limitations have motivated the development of the MLM-DRM framework, which incorporates layer-specific stiffness, damping, geological dip angles, and oblique seismic incidence enabling realistic simulation of tunnel response under complex geological and fault-rupture conditions.

Despite substantial advances in numerical modeling techniques including multi-scale FEM approaches, hybrid FEM-BEM formulations, improved input-motion schemes, and enhanced DRM variants, rigorous treatment of asynchronous seismic excitations and accurate modeling of 3D wave-passage effects remain challenging. Existing studies often rely on vertically propagating waves, simplified phase-shift functions, or the use of quasi-3D input motions that unable to fully capture the spatially varying wavefield generated by finite-fault rupture. Moreover, the earlier research studies have examined only the 2D plane-strain response of underground tunnels (Lin et al., 2010; Wang et al., 2023). However, the 2D analyses cannot evaluate the 3D longitudinal deformations, particularly in regions where the material properties vary along the tunnel alignment or near fault zones, where the wavefield becomes highly complex due to presence of body waves and surface waves. This gap is significant, as asynchronous rupture can induce pronounced differential motion along the tunnel axis, amplify lining stresses, and modify the propagation of body and surface waves in heterogeneous geological conditions.

The present study develops and applies the MLM-DRM framework capable of modeling asynchronous seismic wavefields generated by oblique fault rupture and their interaction with tunnels embedded in inclined layered geology. The proposed framework incorporates layer-specific material properties, oblique incidence angles of 30° and 45°, and a mathematically rigorous asynchronous ground motions, enabling realistic assessment of tunnel response under complex wave-propagation environments. The study is organized as follows: Section 2 presents the mathematical framework of the MLM-DRM and Section 3 describes the generation of asynchronous seismic ground motion using Green's function. Section 4 provides verification studies to confirm the accuracy and reliability of the proposed formulation. Section 5 outlines the comprehensive parametric studies conducted considering variations in fault inclination, geological dip angles, and tunnel cross-section geometry, followed by detailed results and discussion. Finally, Section 6 gives conclusions highlighting the implication of incorporating

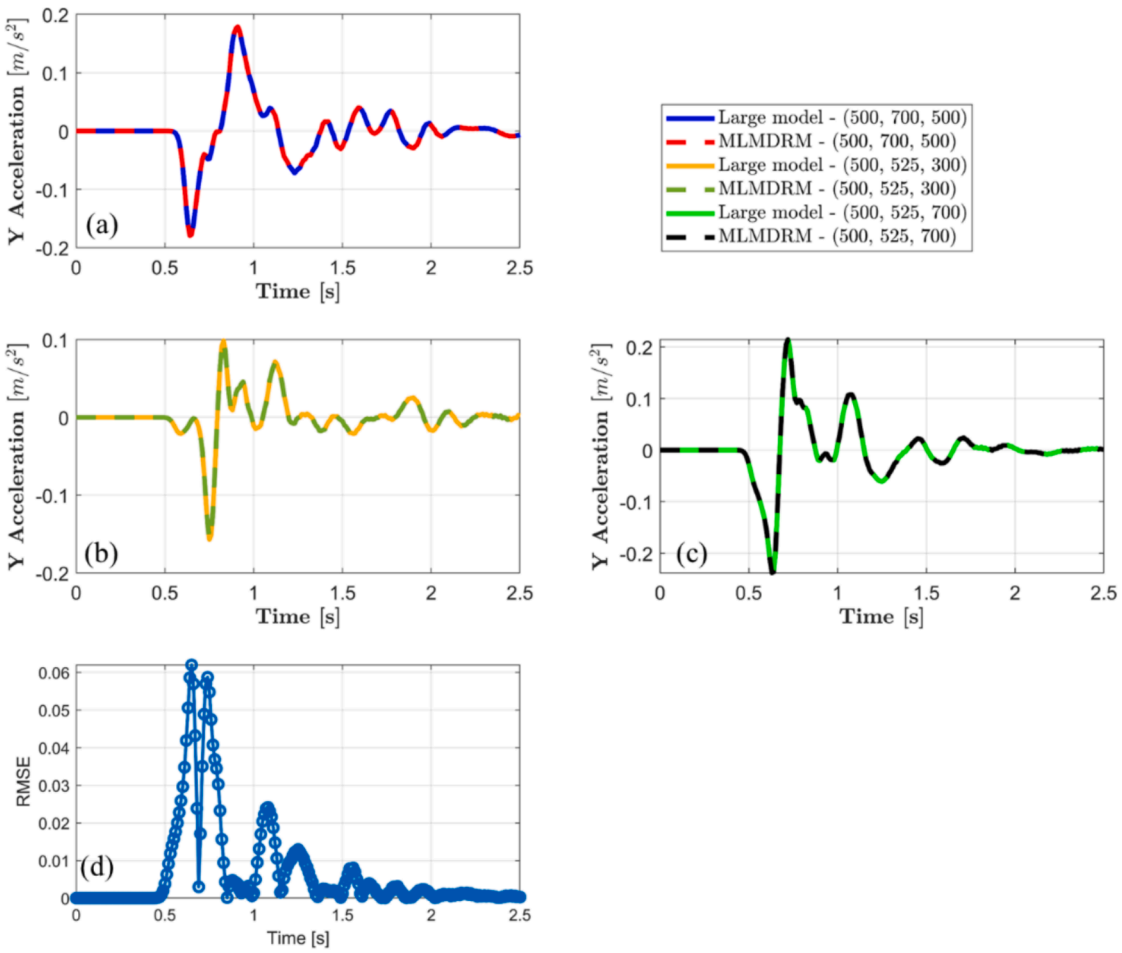


Fig. 8. Comparison of Y-direction acceleration component obtained from the large and reduced models (MLM-DRM) at (a) [X = 500 m, Y = 700 m, Z = 500 m], (b) [X = 500 m, Y = 525 m, Z = 300 m], (c) [X = 500 m, Y = 525 m, Z = 700 m], and (d) Root mean square error (RMSE) between the two models.

asynchronous wave passage effects and layered-geology in the seismic design of tunnels and underground structures.

2. Formulation of MLM-DRM for inclined layered media

A multi-layer modified domain reduction method (MLM-DRM) is developed in this section for the governing equation of the multi-layered inclined media having a tunnel in the domain. Bielak et al. (2003) developed the DRM for seismic analysis of large-scale numerical simulations, accounting for seismic sources (such as faults), wave propagation paths, and the impact of local complex structures, including geological variations (see Fig. 1(a)). Further, Yoshimura et al. (2003) verified the accuracy of the DRM using Green's function approach. The DRM is a two-stage computational approach aimed at reducing the size of the numerical domain through a transformation of the governing equations. In the first stage, the seismic excitation is simulated in the background domain (Fig. 1(b)), and the free-field displacement response together with the effective forces acting on a single-element DRM interface are evaluated and stored. In the second stage, these pre-computed DRM interface forces are imposed on the reduced computational model containing the localized region of interest (Fig. 1(c)). The governing equation of motion for the tunnel problem in geologic media is written as

$$M_G^{\Omega}\ddot{u} + C_G^{\Omega}\dot{u} + K_G^{\Omega}u = F_{ext} \tag{1}$$

where M_G^{Ω}, C_G^{Ω}, K_G^{Ω} and F_{ext} denote the global mass, damping, and stiffness matrices of the domain, and external force terms, respectively, and superscript index Ω indicates the heterogeneous soil region. The equations of sub-matrices for the sub-domains Ω, and Ω^+ are expressed as

$$\begin{bmatrix} M_{ii}^{\Omega} & M_{ib}^{\Omega} \\ M_{bi}^{\Omega} & M_{bb}^{\Omega} \end{bmatrix} \begin{bmatrix} \ddot{u}_i \\ \ddot{u}_b \end{bmatrix} + \begin{bmatrix} C_{ii}^{\Omega} & C_{ib}^{\Omega} \\ C_{bi}^{\Omega} & C_{bb}^{\Omega} \end{bmatrix} \begin{bmatrix} \dot{u}_i \\ \dot{u}_b \end{bmatrix} + \begin{bmatrix} K_{ii}^{\Omega} & K_{ib}^{\Omega} \\ K_{bi}^{\Omega} & K_{bb}^{\Omega} \end{bmatrix} \begin{bmatrix} u_i \\ u_b \end{bmatrix} = \begin{bmatrix} 0 \\ F_b \end{bmatrix} \text{ in } \Omega \tag{2}$$

$$\begin{bmatrix} M_{bb}^{\Omega^+} & M_{be}^{\Omega^+} \\ M_{eb}^{\Omega^+} & M_{ee}^{\Omega^+} \end{bmatrix} \begin{bmatrix} \ddot{u}_b \\ \ddot{u}_e \end{bmatrix} + \begin{bmatrix} C_{bb}^{\Omega^+} & C_{be}^{\Omega^+} \\ C_{eb}^{\Omega^+} & C_{ee}^{\Omega^+} \end{bmatrix} \begin{bmatrix} \dot{u}_b \\ \dot{u}_e \end{bmatrix} + \begin{bmatrix} K_{bb}^{\Omega^+} & K_{be}^{\Omega^+} \\ K_{eb}^{\Omega^+} & K_{ee}^{\Omega^+} \end{bmatrix} \begin{bmatrix} u_b \\ u_e \end{bmatrix} = \begin{bmatrix} -F_b \\ F_e \end{bmatrix} \text{ in } \Omega^+ \tag{3}$$

where subscripts b, i, and e indices denote the boundary, interior, and exterior nodes, respectively; $\ddot{u}_i$, $\dot{u}_i$, u_i, are the acceleration, velocity, and displacement fields within the domain, respectively. The artificial interfaces Γ_b and Γ_e, partition the computational domain into two sub-domains, denoted by Ω and Ω^+. The global matrix equation for the complete system is obtained by adding Eqs. (2) and (3) over the nodes

common to both subdomains (see Fig. 1(a)), and is expressed as

$$\begin{bmatrix} M_{ii}^{\Omega} & M_{ib}^{\Omega} & \ominus \\ M_{bi}^{\Omega} & M_{bb}^{\Omega}+M_{bb}^{\Omega^+} & M_{be}^{\Omega^+} \\ \ominus & M_{eb}^{\Omega^+} & M_{ee}^{\Omega^+} \end{bmatrix} \begin{bmatrix} \ddot{u}_i \\ \ddot{u}_b \\ \ddot{u}_e \end{bmatrix} + \begin{bmatrix} C_{ii}^{\Omega} & C_{ib}^{\Omega} & \ominus \\ C_{bi}^{\Omega} & C_{bb}^{\Omega}+C_{bb}^{\Omega^+} & C_{be}^{\Omega^+} \\ \ominus & C_{eb}^{\Omega^+} & C_{ee}^{\Omega^+} \end{bmatrix} \begin{bmatrix} \dot{u}_i \\ \dot{u}_b \\ \dot{u}_e \end{bmatrix} + \begin{bmatrix} K_{ii}^{\Omega} & K_{ib}^{\Omega} & \ominus \\ K_{bi}^{\Omega} & K_{bb}^{\Omega}+K_{bb}^{\Omega^+} & K_{be}^{\Omega^+} \\ \ominus & K_{eb}^{\Omega^+} & K_{ee}^{\Omega^+} \end{bmatrix} \begin{bmatrix} u_i \\ u_b \\ u_e \end{bmatrix} = \begin{bmatrix} 0 \\ 0 \\ F_e \end{bmatrix} \tag{4}$$

where $\ominus \in \mathbb{R}^{n_i \times n_e}$ denotes a null matrix, where n_i and n_e represent the total numbers of degrees of freedom associated with the interior and exterior boundary nodes, respectively. To transfer the earthquake ground motions generated by the asynchronous seismic source F_e to the artificial boundaries (Γ_b and Γ_e), a free-field (FF) analysis is performed (Fig. 1(b)). In this auxiliary problem, the localized region of interest is removed and replaced by the background medium, which is denoted by Ω^o. The corresponding free-field nodal displacements and boundary forces in Ω^o are denoted by u_b^o, u_i^o, u_e^o, and F_b^o, respectively. The equation of motion governing the exterior domain Ω^+ in the free-field analysis is expressed as

$$\begin{bmatrix} M_{bb}^{\Omega^+} & M_{be}^{\Omega^+} \\ M_{eb}^{\Omega^+} & M_{ee}^{\Omega^+} \end{bmatrix} \begin{bmatrix} \ddot{u}_b^o \\ \ddot{u}_e^o \end{bmatrix} + \begin{bmatrix} C_{bb}^{\Omega^+} & C_{be}^{\Omega^+} \\ C_{eb}^{\Omega^+} & C_{ee}^{\Omega^+} \end{bmatrix} \begin{bmatrix} \dot{u}_b^o \\ \dot{u}_e^o \end{bmatrix} + \begin{bmatrix} K_{bb}^{\Omega^+} & K_{be}^{\Omega^+} \\ K_{eb}^{\Omega^+} & K_{ee}^{\Omega^+} \end{bmatrix} \begin{bmatrix} u_b^o \\ u_e^o \end{bmatrix} = \begin{bmatrix} -F_b^o \\ F_e \end{bmatrix} \text{ in } \Omega^+ \tag{5}$$

The second row in Eq. (5) is reformulated using the free-field quantities evaluated at the boundary Γ_e, which allows the seismic excitation F_e to be expressed explicitly, as

$$F_e = M_{eb}^{\Omega^+}\ddot{u}_b^o + M_{ee}^{\Omega^+}\ddot{u}_e^o + C_{eb}^{\Omega^+}\dot{u}_b^o + C_{ee}^{\Omega^+}\dot{u}_e^o + K_{eb}^{\Omega^+}u_b^o + K_{ee}^{\Omega^+}u_e^o \tag{6}$$

The total displacement vector at the exterior boundary, u_e, is decomposed into the superposition of the free-field displacement u_e^o and a residual component w_e arising from wave scattering induced by the tunnel as follows:

$$u_e = u_e^o + w_e \tag{7}$$

Substituting this decomposition (Eq. (7)) into Eq. (4) and rearranging the terms by moving the free-field contributions to the right-hand side, yields the modified governing equation as

$$\begin{bmatrix} M_{ii}^{\Omega} & M_{ib}^{\Omega} & \ominus \\ M_{bi}^{\Omega} & M_{bb}^{\Omega}+M_{bb}^{\Omega^+} & M_{be}^{\Omega^+} \\ \ominus & M_{eb}^{\Omega^+} & M_{ee}^{\Omega^+} \end{bmatrix} \begin{bmatrix} \ddot{u}_i \\ \ddot{u}_b \\ \ddot{w}_e \end{bmatrix} + \begin{bmatrix} C_{ii}^{\Omega} & C_{ib}^{\Omega} & \ominus \\ C_{bi}^{\Omega} & C_{bb}^{\Omega}+C_{bb}^{\Omega^+} & C_{be}^{\Omega^+} \\ \ominus & C_{eb}^{\Omega^+} & C_{ee}^{\Omega^+} \end{bmatrix} \begin{bmatrix} \dot{u}_i \\ \dot{u}_b \\ \dot{w}_e \end{bmatrix} + \begin{bmatrix} K_{ii}^{\Omega} & K_{ib}^{\Omega} & \ominus \\ K_{bi}^{\Omega} & K_{bb}^{\Omega}+K_{bb}^{\Omega^+} & K_{be}^{\Omega^+} \\ \ominus & K_{eb}^{\Omega^+} & K_{ee}^{\Omega^+} \end{bmatrix} \begin{bmatrix} u_i \\ u_b \\ w_e \end{bmatrix} = \begin{bmatrix} 0 \\ -M_{be}^{\Omega^+}\ddot{u}_e^o - C_{be}^{\Omega^+}\dot{u}_e^o - K_{be}^{\Omega^+}u_e^o \\ -M_{ee}^{\Omega^+}\ddot{u}_e^o - C_{ee}^{\Omega^+}\dot{u}_e^o - K_{ee}^{\Omega^+}u_e^o + F_e \end{bmatrix} \tag{8}$$

Further substitution of Eq. (6) into Eq. (8), the final dynamic equations of equilibrium of the systems are expressed as

$$\begin{bmatrix} M_{ii}^{\Omega} & M_{ib}^{\Omega} & \ominus \\ M_{bi}^{\Omega} & M_{bb}^{\Omega}+M_{bb}^{\Omega^+} & M_{be}^{\Omega^+} \\ \ominus & M_{eb}^{\Omega^+} & M_{ee}^{\Omega^+} \end{bmatrix} \begin{bmatrix} \ddot{u}_i \\ \ddot{u}_b \\ \ddot{w}_e \end{bmatrix} + \begin{bmatrix} C_{ii}^{\Omega} & C_{ib}^{\Omega} & \ominus \\ C_{bi}^{\Omega} & C_{bb}^{\Omega}+C_{bb}^{\Omega^+} & C_{be}^{\Omega^+} \\ \ominus & C_{eb}^{\Omega^+} & C_{ee}^{\Omega^+} \end{bmatrix} \begin{bmatrix} \dot{u}_i \\ \dot{u}_b \\ \dot{w}_e \end{bmatrix} + \begin{bmatrix} K_{ii}^{\Omega} & K_{ib}^{\Omega} & \ominus \\ K_{bi}^{\Omega} & K_{bb}^{\Omega}+K_{bb}^{\Omega^+} & K_{be}^{\Omega^+} \\ \ominus & K_{eb}^{\Omega^+} & K_{ee}^{\Omega^+} \end{bmatrix} \begin{bmatrix} u_i \\ u_b \\ w_e \end{bmatrix} = \begin{bmatrix} 0 \\ -M_{be}^{\Omega^+}\ddot{u}_e^o - C_{be}^{\Omega^+}\dot{u}_e^o - K_{be}^{\Omega^+}u_e^o \\ M_{eb}^{\Omega^+}\ddot{u}_b^o + C_{eb}^{\Omega^+}\dot{u}_b^o + K_{eb}^{\Omega^+}u_b^o \end{bmatrix} \tag{9}$$

The mass, damping, and stiffness matrices appearing on the left-hand side of Eq. (9) remain identical to those in Eq. (4). Consequently, the original seismic force vector F_e is replaced by an equivalent set of effective nodal forces, F^{eff}, as defined in Eq. (10):

$$F^{eff} = \begin{bmatrix} F_i^{eff} \\ F_b^{eff} \\ F_e^{eff} \end{bmatrix} = \begin{bmatrix} 0 \\ -M_{be}^{\Omega^+}\ddot{u}_e^o - C_{be}^{\Omega^+}\dot{u}_e^o - K_{be}^{\Omega^+}u_e^o \\ M_{eb}^{\Omega^+}\ddot{u}_b^o + C_{eb}^{\Omega^+}\dot{u}_b^o + K_{eb}^{\Omega^+}u_b^o \end{bmatrix} \tag{10}$$

The coupling submatrices $M_{be}^{\Omega^+}$, $K_{be}^{\Omega^+}$, $C_{be}^{\Omega^+}$, $M_{eb}^{\Omega^+}$, $K_{eb}^{\Omega^+}$ and $C_{eb}^{\Omega^+}$ appearing in Eq. (10) are zero throughout the exterior domain Ω^+ (see Fig. 1(b)), except at the artificial boundary elements that include nodes located on the interfaces Γ_e and Γ_b. The MLM-DRM is a robust two-step algorithm for transferring far-field seismic ground motion to near-field localized regions. Furthermore, the computation of effective seismic forces relies solely on the displacement at the DRM boundary nodes which significantly reduces the memory requirement of the algorithm. This also eliminates the need to store or process the entire displacement

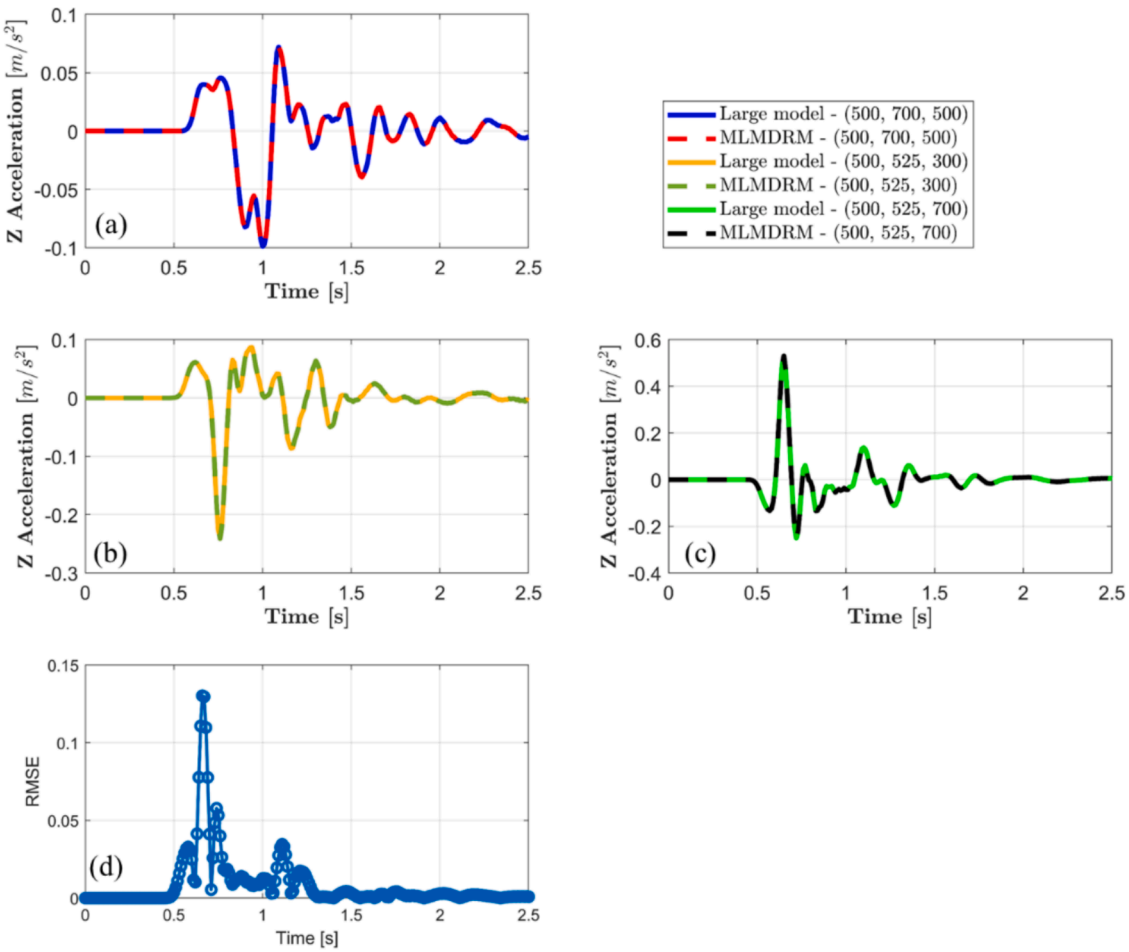


Fig. 9. Comparison of Z-direction acceleration component obtained from the large and reduced models (MLM-DRM) at (a) [X = 500 m, Y = 700 m, Z = 500 m], (b) [X = 500 m, Y = 525 m, Z = 300 m], (c) [X = 500 m, Y = 525 m, Z = 700 m], and (d) Root mean square error (RMSE) between the two models.

field of the large-scale model. The effective seismic forces are transferred to the smaller computational domain. Moreover, the reduced model proves to be highly beneficial for conducting parametric analyses and investigating the nonlinear and inelastic behavior of the tunnel. Finally, the reduced system of governing equations (Eq. (10)) is solved to obtain the displacement field using the Newmark-β time integration scheme.

3. Generation of asynchronous ground motion using rupture delay model

Asynchronous ground motion modeling is incorporated directly in the mathematical formulation by considering spatially varying incident wavefields generated by the fault rupture. This allows the MLM-DRM framework to capture differential motions, wave-passage effects, phase delays, and out-of-plane variations that arise naturally in layered media subjected to obliquely incident primary (P) and shear (S) waves. The resulting formulation forms the theoretical foundation for the numerical implementation presented in this section. These asynchronous ground motions are used in the verification study (Section 4) and parametric sensitivity analyses (Section 5) involving different geological configurations and fault-inclination scenarios.

3.1. Moment-tensor and equivalent body forces

A moment-tensor point source at location at $\mathbf{x}_s$ with components $M_{ij}(t;\mathbf{x}_s)$ is equivalent to the body force as

$$f_i(\mathbf{x},t) = -\sum_j \partial_j \left(M_{ij}(t;\mathbf{x}_s)\,\delta(\mathbf{x}-\mathbf{x}_s) \right) \tag{11}$$

where ∂_j is $\partial/\partial x_j$ and $\delta(\cdot)$ is the Dirac delta function. This is the classical representation used for coupling moment tensors to elastodynamic wave propagation (Aki and Richards, 2002).

3.2. Displacement field via elastodynamic Green's functions

Let $G_{ki}(\mathbf{x},t;\mathbf{x}_s)$ denote the displacement Green's tensor. Using Eq. (11) and integrating by parts, the displacement component u_k generated by a moment tensor is expressed as

$$u_k(\mathbf{x},t) = \sum_{i,j} \int_0^t G_{ki,j}(\mathbf{x},t-\tau;\mathbf{x}_s)\, M_{ij}(\tau;\mathbf{x}_s)\, d\tau \tag{12}$$

where $G_{ki,j}$ denotes derivative of G_{ki} with respect to the source coordinate $\boldsymbol{x}_{s,j}$:

$$G_{ki,j}(\mathbf{x},t;\mathbf{x}_s) = \frac{\partial}{\partial x_{s,j}} G_{ki}(\mathbf{x},t;\mathbf{x}_s)$$

For multiple point sources distributed over a fault surface S, the displacement becomes

$$u_k(\mathbf{x},t) = \iint_S \sum_{i,j} \int_0^t G_{ki,j}(\mathbf{x},t-\tau;\mathbf{x}_s)\, M_{ij}(\tau;\mathbf{x}_s)\, d\tau\, dS(\mathbf{x}_s) \tag{13}$$

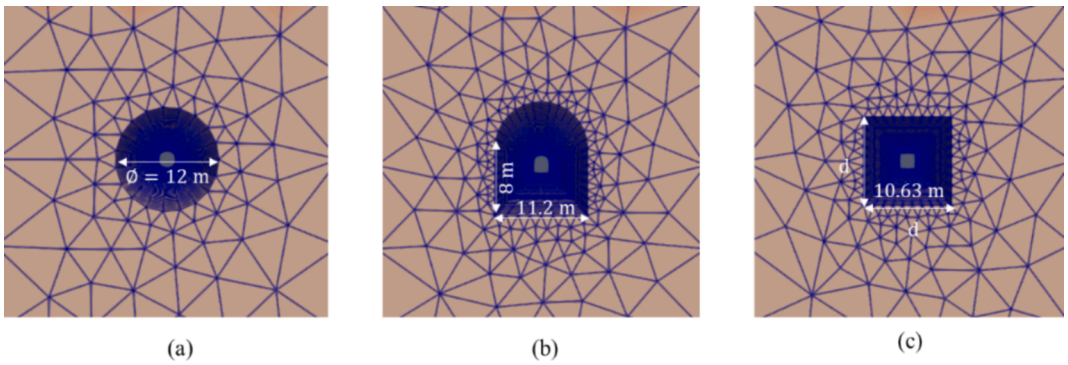


Fig. 10. Tunnel sections considered in the study: (a) Circular, (b) Horseshoe, and (c) Square.

3.3. Traction by moment-tensor

The traction component, $t_\alpha(x_b, t)$ at a boundary point $\mathbf{x}_b$ is obtained using a traction kernel $T_{\alpha i j}$ as

$$t_\alpha(\mathbf{x}_b, t) = \sum_{ij} \int_0^t T_{\alpha i j}(\mathbf{x}_b, t-\tau; \mathbf{x}_s)\, M_{ij}(\tau; \mathbf{x}_s)\, d\tau \tag{14}$$

This traction provides the time-dependent Neumann boundary data required for the DRM. The kernel T is derived from spatial derivatives of the Green's tensor and the elastic stiffness matrix.

3.4. Moment tensor and rupture-delay model

For asynchronous fault rupture, each point source $\mathbf{x}_s$ begins radiating after a delay as

$$t_d(\mathbf{x}_s) = \frac{D(\mathbf{x}_s)}{V_r}, D(\mathbf{x}_s) = \left\| \mathbf{x}_s - \mathbf{x}_r \right\| \tag{15}$$

where $\mathbf{x}_r$ is the rupture nucleation point and V_r is the rupture velocity. Thus, the local moment history becomes a shifted and directionally modulated version of the source-time function:

$$M_{ij}(t; \mathbf{x}_s) = \mathrm{A}_{ij}(\theta, \lambda, \Phi_s)\, M_0(t - t_d(\mathbf{x}_s))\, H(t - t_d(\mathbf{x}_s)) \tag{16}$$

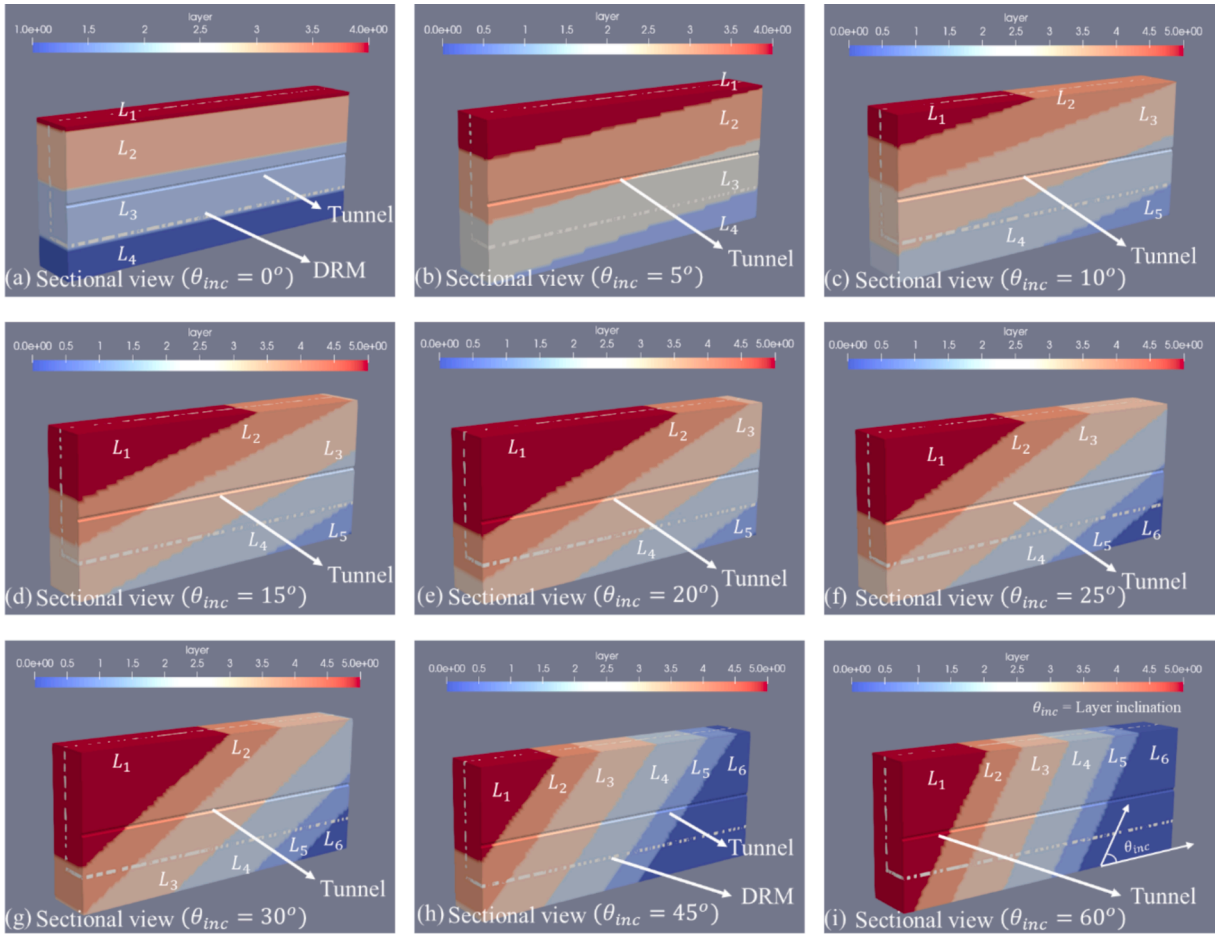


Fig. 11. Different inclined layered geologic media: (a) $\theta_{inc} = 0^o$, (b) $\theta_{inc} = 5^o$, (c) $\theta_{inc} = 10^o$, (d) $\theta_{inc} = 15^o$, (e) $\theta_{inc} = 20^o$, (f) $\theta_{inc} = 25^o$, (g) $\theta_{inc} = 30^o$, (h) $\theta_{inc} = 45^o$, and (i) $\theta_{inc} = 60^o$.

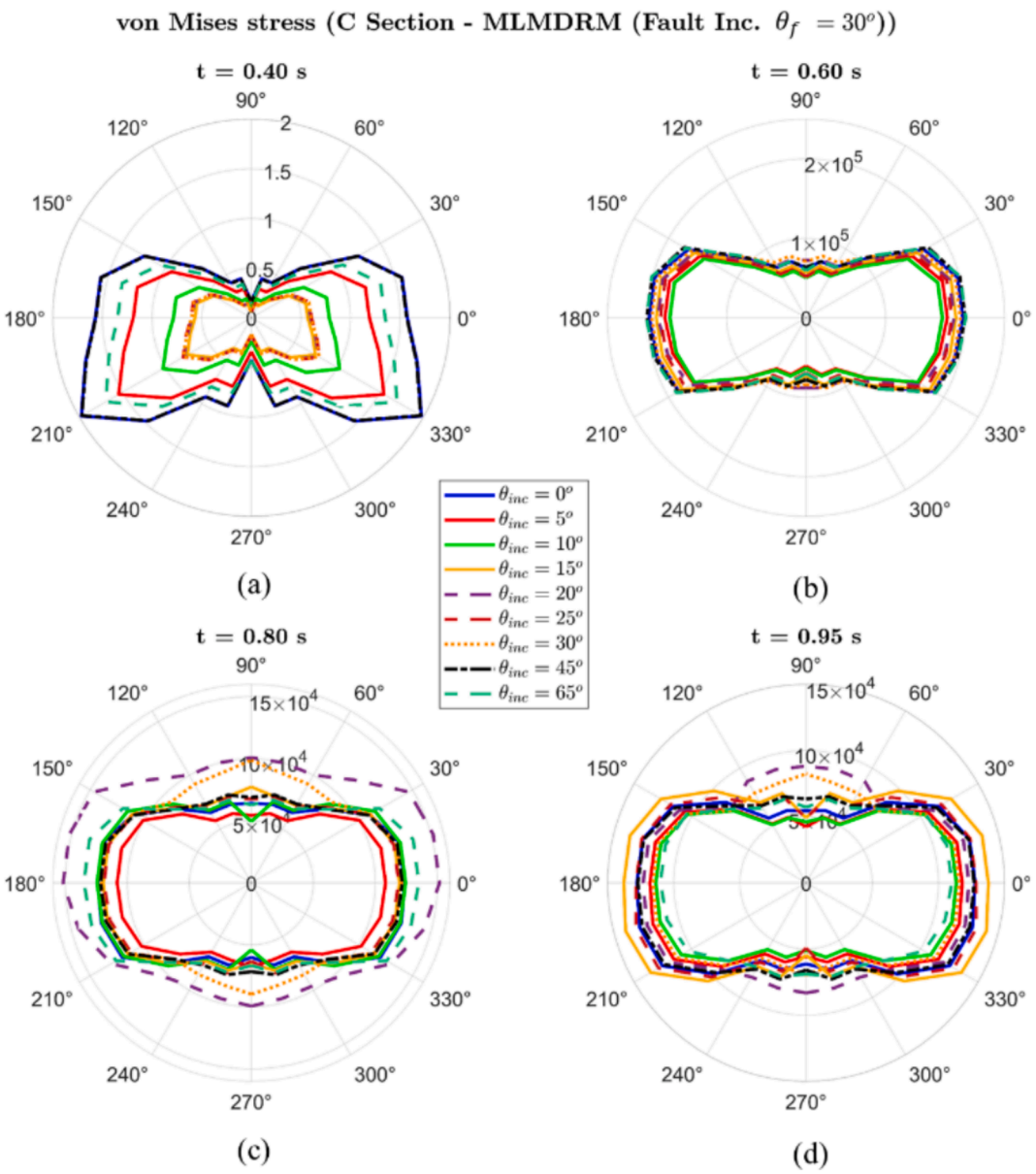


Fig. 12. Variation of von Mises stresses for different soil media around the circular section for fault inclined at $\theta_f = 30^o$: (a) t = 0.40 s, (b) t = 0.60 s, (c) t = 0.80 s, and (d) t = 0.95 s.

where $A_{ij}(\theta, \lambda, \Phi_s)$ are the angular radiation coefficients depending on dip θ, rake λ, and strike Φ_s; and $H(\cdot)$ is the Heaviside step function.

3.4.1. Moment-tensor components

The seismic moment $M_0(t)$ is transformed into the global coordinate system (X, Y, Z), where the Z-axis is vertical and the Y-axis aligned with the strike direction (see Fig. 2). The resulting moment can be expressed in the form of a symmetric matrix of size 3×3 (Aki and Richards, 2002). The components of the seismic moment tensor, combined with the delayed source time function and radiation coefficients $A_{ij}(\theta, \lambda, \Phi_s)$ give the explicit moment-tensor components as in Eqs. (17)–(22):

$$M_{XX}(t;\mathbf{x}_s) = -M_0(t - t_d\mathbf{x}_s)\left(\sin\theta\cos\lambda\sin2\Phi_s + \sin2\theta\sin\lambda sin^2\Phi_s\right) \tag{17}$$

$$\begin{aligned} M_{XY}(t;\mathbf{x}_s) &= M_0(t - t_d\mathbf{x}_s)\left(\sin\theta\cos\lambda\cos2\Phi_s + \frac{1}{2}\sin2\theta\sin\lambda\sin2\Phi_s\right) \\ &= M_{YX}(t;\mathbf{x}_s) \end{aligned} \tag{18}$$

$$\begin{aligned} M_{XZ}(t;\mathbf{x}_s) &= -M_0(t - t_d\mathbf{x}_s)(\cos\theta\cos\lambda\cos\Phi_s + \cos2\theta\sin\lambda\sin2\Phi_s) \\ &= M_{ZX}(t;\mathbf{x}_s) \end{aligned} \tag{19}$$

$$M_{YY}(t;\mathbf{x}_s) = M_0(t - t_d\mathbf{x}_s)\left(\sin\theta\cos\lambda\sin2\Phi_s - \sin2\theta\sin\lambda cos^2\Phi_s\right) \tag{20}$$

$$M_{YZ}(t;\mathbf{x}_s) = -M_0(t - t_d\mathbf{x}_s)(\cos\theta\cos\lambda\sin\Phi_s - \cos2\theta\sin\lambda\cos\Phi_s) = M_{ZY}(t;\mathbf{x}_s) \tag{21}$$

$$M_{ZZ}(t;\mathbf{x}_s) = M_0(t - t_d\mathbf{x}_s)(\sin2\theta\sin\lambda) \tag{22}$$

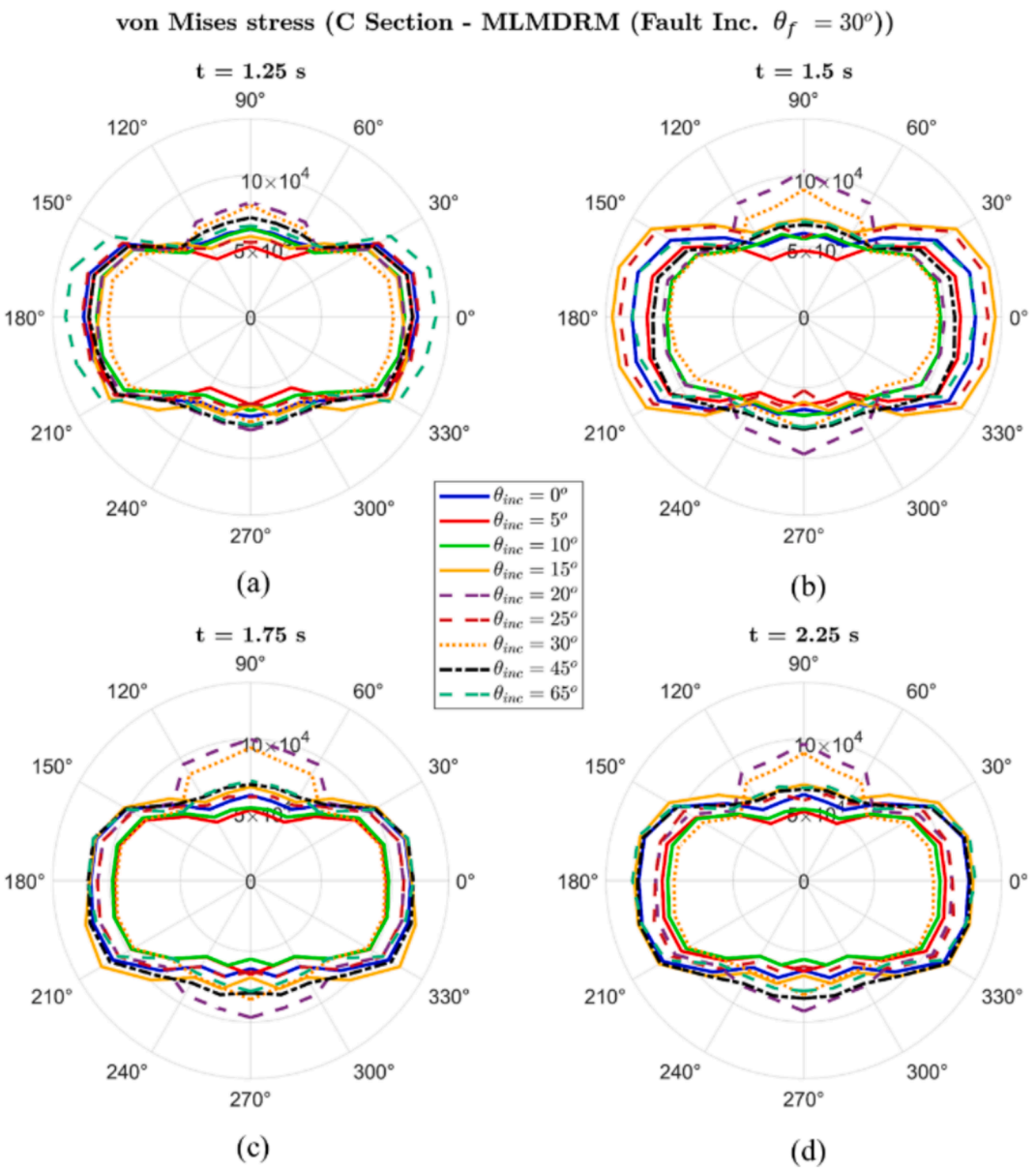


Fig. 13. Variation of von Mises stresses for different soil media around the circular section for fault inclined at $\theta_f = 30^o$: (a) t = 1.25 s, (b) t = 1.50 s, (c) t = 1.75 s, and (d) t = 2.25 s.

These expressions are used to obtained the subsequent equations as in Eqs. (24)-(27).

3.5. Final displacements after rupture delay

Substituting Eq. (16) into Eq. (12) gives

$$u_k(\mathbf{x},t) = \sum_{i,j} \mathrm{A}_{ij}(\theta,\lambda,\Phi_s) \int_{t_d(\mathbf{x}_s)}^{t} G_{ki,j}(\mathbf{x},t-\tau;\mathbf{x}_s)\, M_0(\tau - t_d(\mathbf{x}_s))\, d\tau.$$

$$= \sum_{i,j} \int_0^t G_{ki,j}(\mathbf{x},t-\tau;\mathbf{x}_s)\, \mathrm{A}_{ij}(\theta,\lambda,\Phi_s)\, M_0(\tau - t_d(\mathbf{x}_s))\, H(\tau - t_d(\mathbf{x}_s))\, d\tau \tag{23}$$

Defining $\eta = \tau - t_d(\mathbf{x}_s)$, the convolution becomes

$$u_k(\mathbf{x},t) = \sum_{i,j} \mathrm{A}_{ij}(\theta,\lambda,\Phi_s) \int_0^{t-t_d(\mathbf{x}_s)} G_{ki,j}(\mathbf{x},t-t_d(\mathbf{x}_s)-\eta;\mathbf{x}_s)\, M_0(\eta)\, d\eta \tag{24}$$

3.6. DRM layer forces at boundary

The DRM layer forces are the final tractions, obtained by inserting

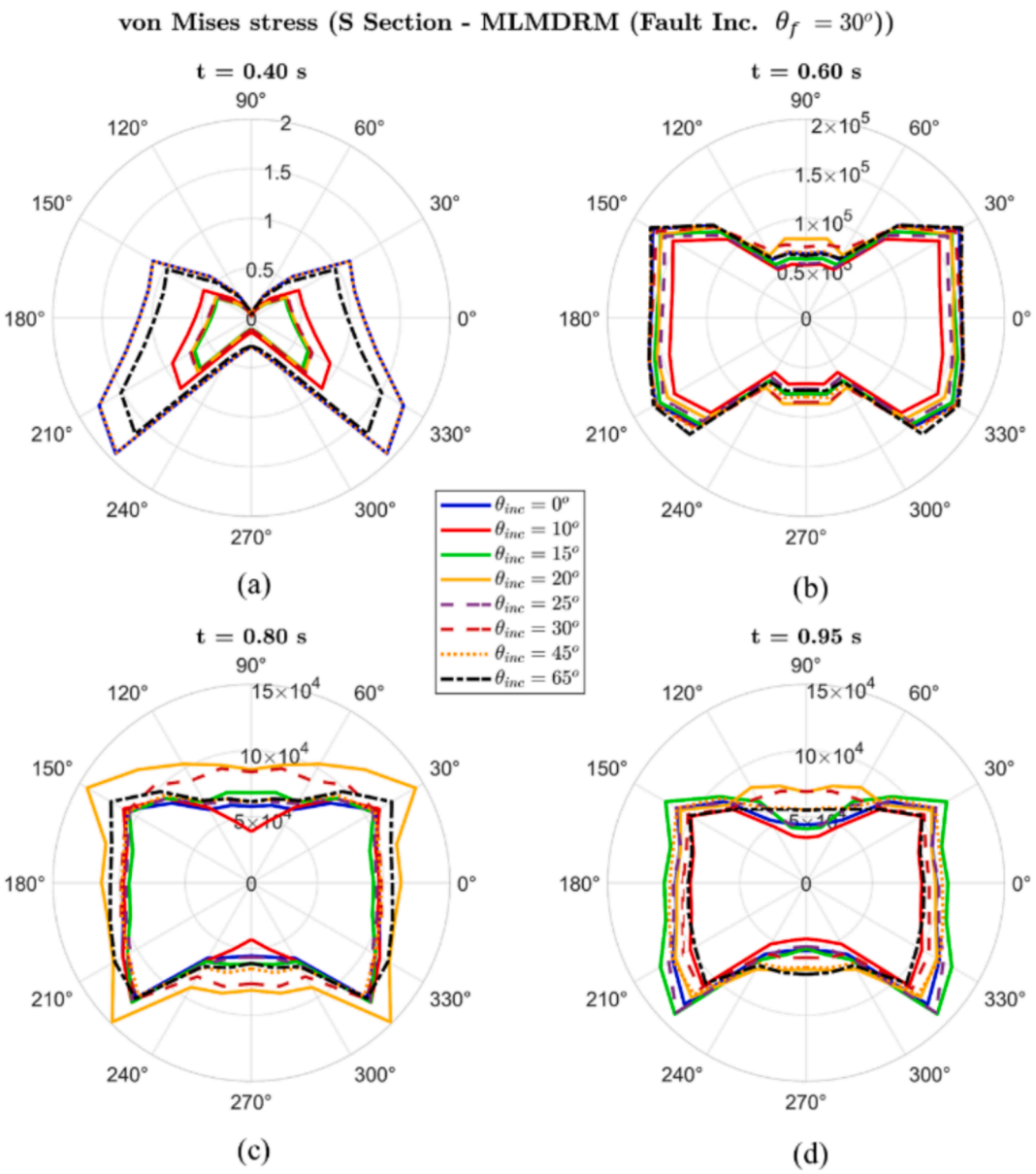


Fig. 14. Variation of von Mises stresses for different soil media around the square section for fault inclined at $\theta_f = 30^o$: (a) t = 0.40 s, (b) t = 0.60 s, (c) t = 0.80 s, and (d) t = 0.95 s.

Eq. (16) in Eq. (14):

$$t_a(\mathbf{x}_b, t) = \sum_{\mathbf{x}_s}\sum_{ij} \mathrm{A}_{ij}(\theta, \lambda, \Phi_s) \int_0^{t-t_d(\mathbf{x}_s)} T_{\alpha ij}(\mathbf{x}_b, t - t_d(\mathbf{x}_s) - \eta; \mathbf{x}_s)\, M_0(\eta)\, d\eta \tag{25}$$

The corresponding finite-element DRM nodal force is obtained from the following equation:

$$F_a(t) = \int_{\Gamma_{\mathrm{DRM}}} N_a(\mathbf{x}_b)\, t(\mathbf{x}_b, t)\, d\Gamma(\mathbf{x}_b) \tag{26}$$

The expression for final DRM forces is expressed as

$$P_a(t) = \sum_{\mathbf{x}_s}\sum_{ij} \mathrm{A}_{ij}(\cdot) \int_0^{t-t_d(\mathbf{x}_s)} \left[\int_{\Gamma_{\mathrm{DRM}}} N_a(\mathbf{x}_b) T_{\alpha ij}(\mathbf{x}_b, t - t_d(\mathbf{x}_s) - \eta; \mathbf{x}_s)\, d\Gamma \right] M_0(\eta)\, d\eta \tag{27}$$

The bracketed term is a precomputable kernel depending only on geometry and elastic properties of the medium.

4. Validation of MLM-DRM with full-scale model

In the present study, all numerical simulations are performed using the open-source finite element platform MASTODON (Multi-hazard Analysis for STOchastic time-DOmaiN phenomena), developed within the Multiphysics Object-Oriented Simulation Environment (MOOSE) framework (Coleman et al., 2017). The seismic response analysis of the tunnel embedded in complex geologic media is carried out using the proposed efficient MLM-DRM framework, whose overall computational workflow is depicted in Fig. 3. The analysis follows a two-stage procedure consisting of a free-field wave propagation analysis (Stage I) and a reduced-domain tunnel response analysis using DRM layer forces (Stage II).

4.1. Stage I: Free-field analysis and seismic source modeling

In Stage I, the free-field seismic response of the ground is evaluated

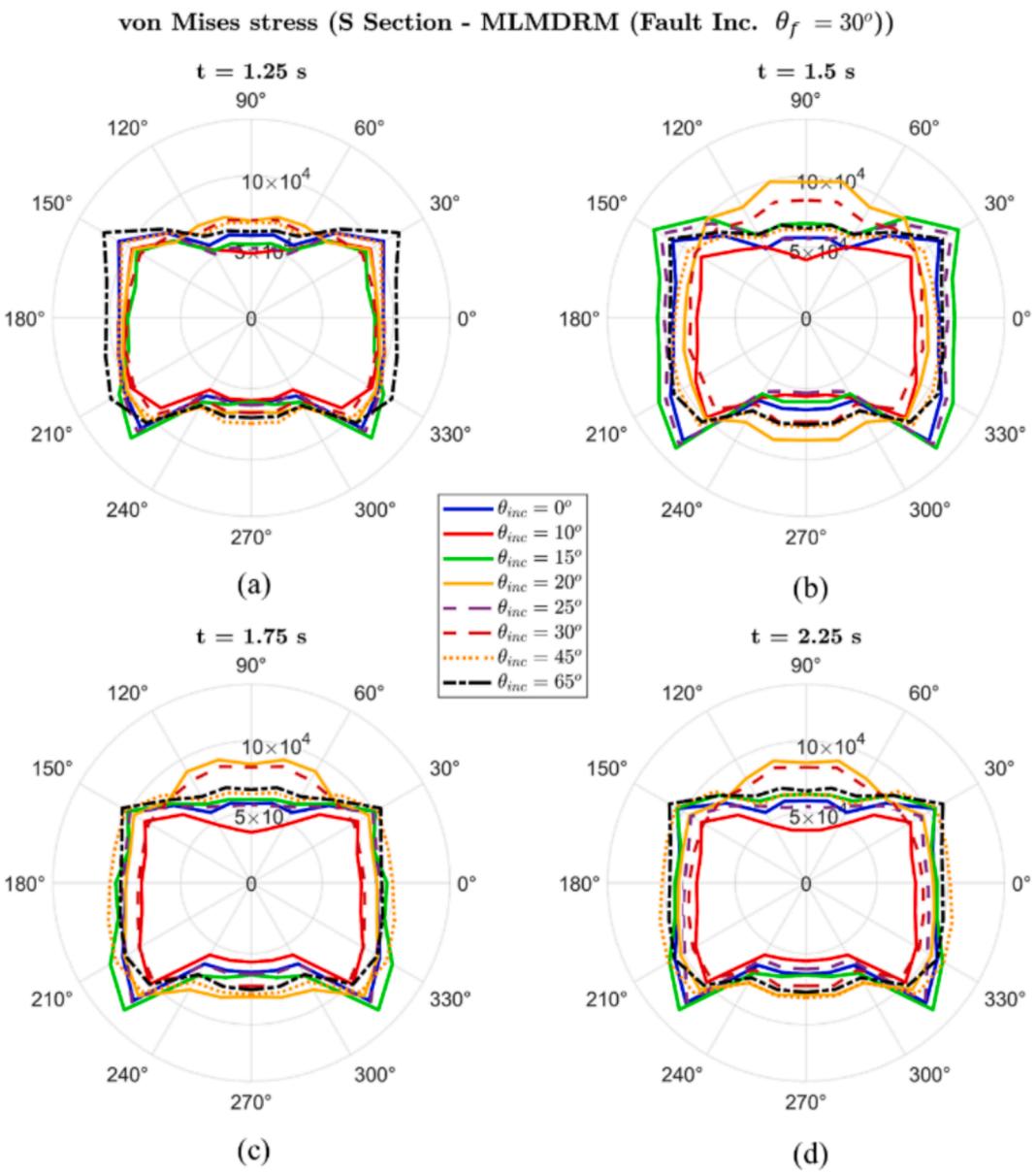


Fig. 15. Variation of von Mises stresses for different soil media around the square section for fault inclined at $\theta_f = 30^o$: (a) t = 1.25 s, (b) t = 1.50 s, (c) t = 1.75 s, and (d) t = 2.25 s.

in the absence of the tunnel to accurately capture fault-induced wave propagation. The corresponding numerical configuration is depicted in Fig. 4(a–c), where 3D domain of dimensions 500 m × 700 m × 1000 m is considered for the analysis. The subsurface is considered as a six-layer stratified media (top to bottom) with shear-wave velocities $V_{S1} = 686$ m/s, $V_{S2} = 745.4$ m/s, $V_{S3} = 858.4$ m/s, $V_{S4} = 974.7$ m/s, $V_{S5} = 1021.5$ m/s, and $V_{S6} = 1414.2$ m/s, and corresponding thicknesses of 110 m, 100 m, 150 m, 150 m, 90 m, and 300 m, respectively. The geological layers are inclined at an angle of $\theta_{inc} = 10°$, allowing realistic representation of wave refraction and transmission across dipping interfaces. The meshes corresponding to the free-field, reduced, and large models are shown in Fig. 5(a–c).

The seismic excitation is generated through an asynchronous fault rupture source model, implemented using the *SeismicSource* module in MASTODON. The fault plane is characterized by a dip angle of 30°, defined as the angle between the fault plane and the horizontal direction, and a rake angle of 90°, corresponding to pure dip-slip motion. The fault slip direction and rupture characteristics are therefore consistent with a reverse faulting mechanism. The elastic response of the fault rupture is governed by a shear modulus of 8.776 GPa, and the rupture process is discretized using 16,032 fault source points, enabling accurate spatial representation of rupture propagation and associated wave radiation. This high-resolution source discretization allows simulation of non-uniform, time-lagged wave arrivals, capturing key features of wave-passage effects, radiation patterns, and directional dependence of seismic loading. The resulting wavefield consists of obliquely incident P-waves, S-waves, and surface waves, as illustrated in the sectional and longitudinal views of the free-field response in Fig. 6(a) and (b), respectively.

4.2. Stage II: Reduced-domain tunnel analysis using MLM-DRM

Following the free-field simulation, displacement, velocity, and acceleration time histories are extracted along the DRM interface, and the corresponding equivalent nodal forces are computed. These forces are subsequently applied to a significantly smaller near-field (reduced) domain with dimensions 150 m × 300 m × 1000 m, as shown in Fig. 6(c, d). This reduced model contains a circular tunnel of diameter 12 m

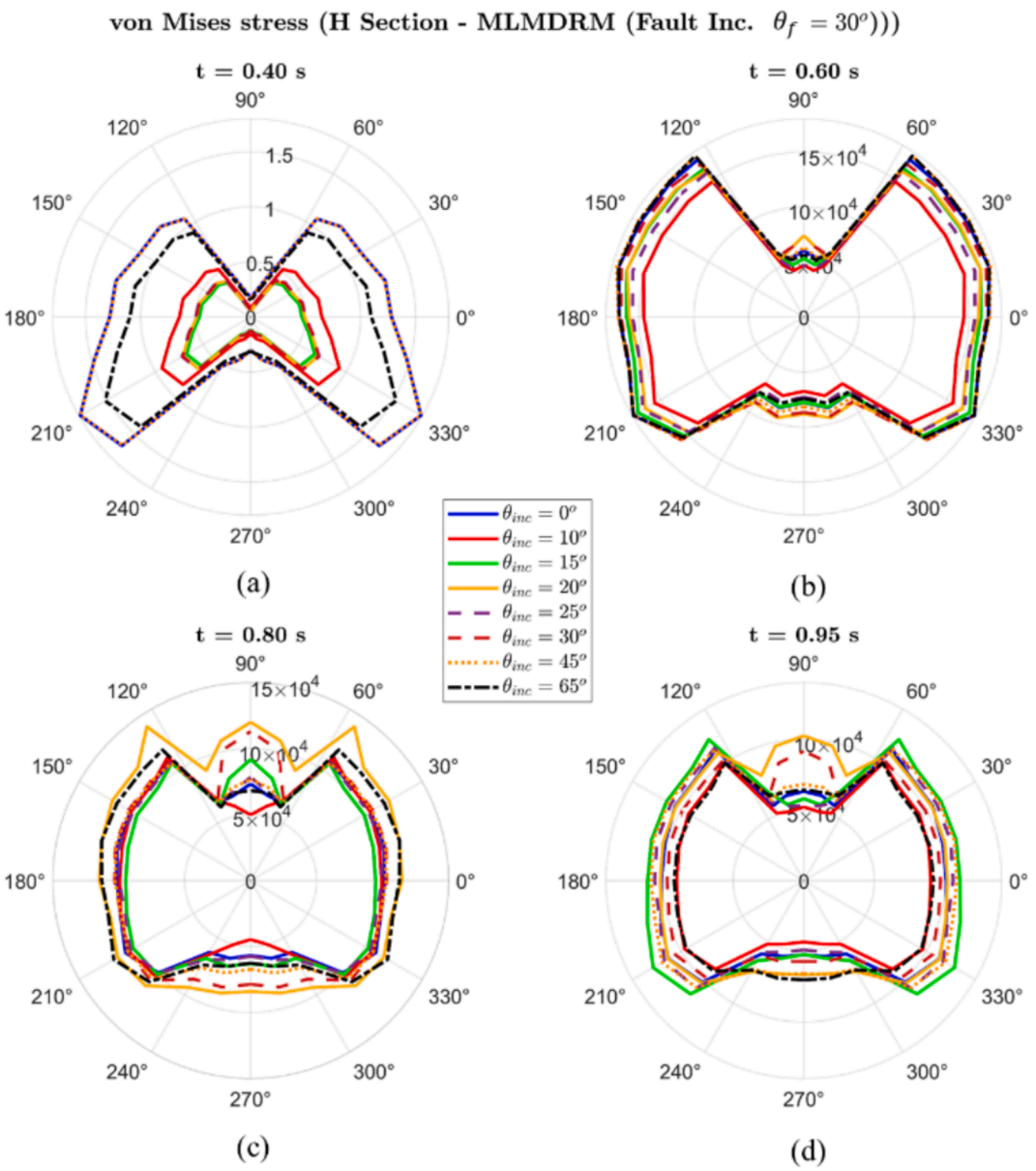


Fig. 16. Variation of von Mises stresses for different soil media around the horseshoe section for fault inclined at $\theta_f = 30^o$: (a) t = 0.40 s, (b) t = 0.60 s, (c) t = 0.80 s, and (d) t = 0.95 s.

embedded within the geologic media, while preserving the essential wave characteristics imposed by the asynchronous fault rupture. A mesh discretization for the reduced model is shown in Fig. 5(b). The tunnel is represented as a hollow cavity within the inclined soil media to examine the influence of layered geology, fault orientation, and asynchronous seismic loading on soil-tunnel interaction. An explicit tunnel lining and its structural behavior are not included; the wave propagation characteristics and kinematic interaction mechanisms are considered effectively. This aspect helps isolate the seismic response by reducing uncertainties related to lining thickness, stiffness, and interface properties. The interaction between the soil and the tunnel boundary is modeled using a common-node approach, ensuring continuity of displacements and stresses across the interface. This approach allows seamless transmission of stresses and deformations, effectively capturing the inherent soil arching behavior without introducing additional interface elements or contact laws.

Dynamic equilibrium equations are solved using the implicit Newmark-β time integration scheme (Newmark, 1959), with parameters $\beta = 0.25$ and $\gamma = 0.5$, ensuring unconditional stability. To mitigate numerical dispersion, a minimum resolution of ten nodes per wavelength is adopted following Ihlenburg and Babuška (1995). Spatial discretization considers 6-node prismatic elements in the vicinity of the tunnel to accurately capture stress concentrations, and 8-node brick elements are used elsewhere in the domain. A Rayleigh damping ratio of 3% is adopted in all simulations to provide adequate numerical energy dissipation and to minimize spurious wave reflections within the computational domain, without significantly affecting the propagating seismic wavefield. Viscous absorbing boundaries (Lysmer and Kuhlemeyer, 1969) are prescribed on all boundaries except the free surface to effectively dissipate the spurious wave reflections, refractions and scattering. The resulting nonlinear system is solved using a preconditioned Jacobian-free Newton-Krylov (JFNK) solver (Ahrabi and Mavriplis, 2020), ensuring robust convergence for large-scale dynamic analyses.

4.3. Validation of MLM-DRM framework

The full-domain simulation as given in Banjare et al. (2025) is

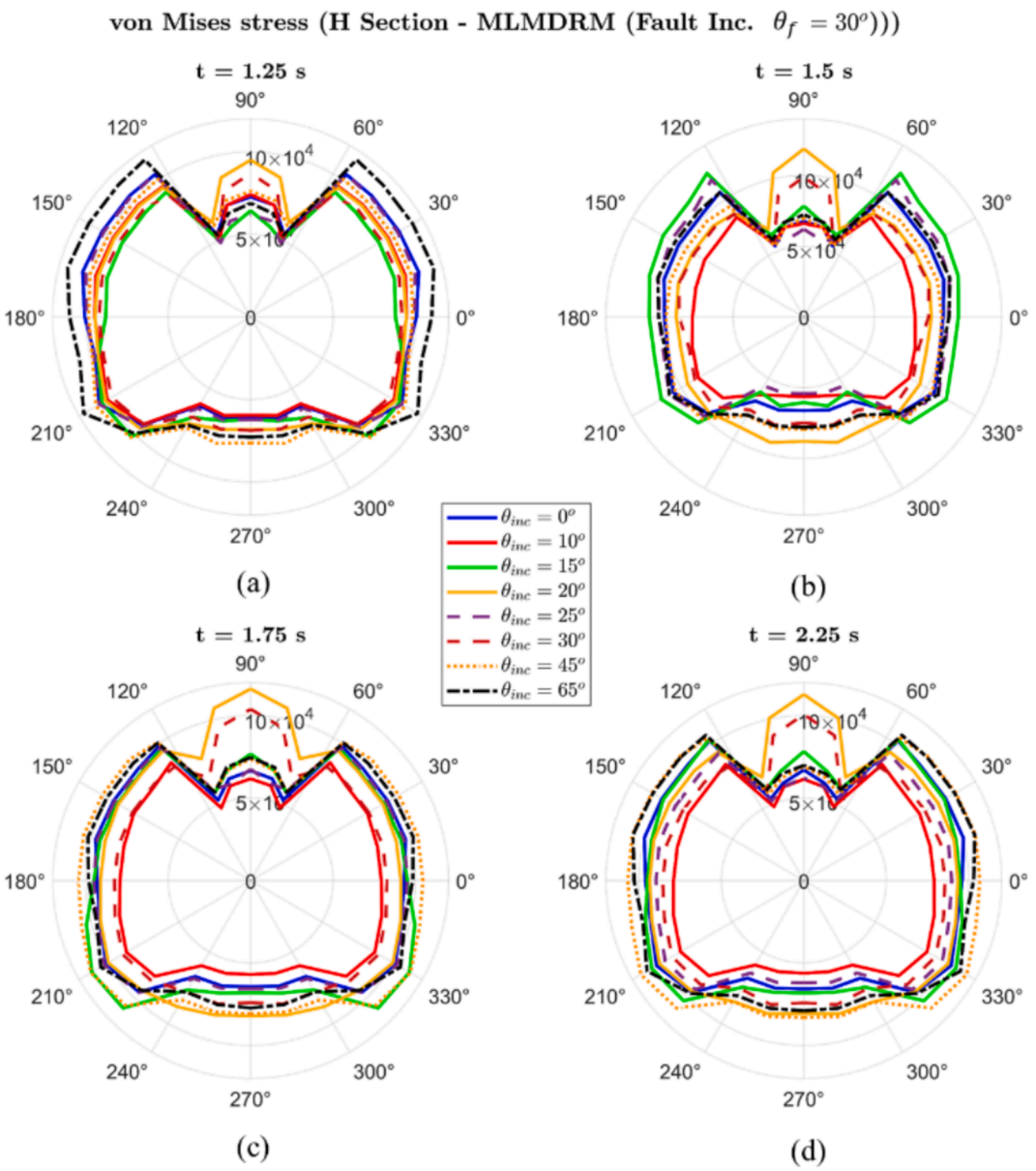


Fig. 17. Variation of von Mises stresses for different soil media around the horseshoe section for fault inclined at $\theta_f = 30^o$: (a) t = 1.25 s, (b) t = 1.50 s, (c) t = 1.75 s, and (d) t = 2.25 s.

considered as a benchmark problem to validate the proposed MLM-DRM framework for inclined geologic media, which explicitly captures seismic source effects, wave propagation, and tunnel interaction within a single computational model. As illustrated in Fig. 4(c) and Fig. 6(e), the large-domain model represents a complete soil–fault–tunnel (SFT) system and is treated as a *benchmark problem* because it directly simulates asynchronous fault rupture and wave propagation without any domain reduction. In contrast, the proposed MLM-DRM framework employs a two-step approach, where the free-field response is first computed (Fig. 4(a), Fig. 6(a-b)), and the resulting equivalent nodal forces are subsequently applied to a reduced domain containing the tunnel (Fig. 4(b), Fig. 6(c-d)). The accuracy of the proposed approach is assessed by comparing the acceleration time histories at representative locations — [X = 500 m, Y = 700 m, Z = 500 m], [X = 500 m, Y = 525 m, Z = 300 m], and [X = 500 m, Y = 525 m, Z = 700 m] between the reduced MLM-DRM model and the benchmark full-domain model, as shown in Fig. 7(a–c), 8(a–c), and 9(a–c), respectively. The corresponding Root Mean Square Error (RMSE) variations are presented in Fig. 7 (d), 8(d), and 9(d). Furthermore, the RMSE values remain very small throughout the simulation duration, indicating minimal deviation between the two models. The close agreement between the two sets of results confirms that the MLM-DRM model accurately reproduces asynchronous wave arrival, wave-passage effects, and resulting tunnel response, demonstrating that the reduced-domain formulation preserves the essential physics of seismic wave propagation in layered media. In addition, the computational efficiency of the MLM-DRM approach is also evaluated. The simulations were run on a Dell Precision workstation equipped with a 13th Generation Intel core i9-13900 K processor using 16 cores. The benchmark full-domain model took around 10 h, while reduced MLM-DRM model took 1.25 h (~ 8X less computational time compared to the full-domain model). Moreover, the full-domain model requires nearly 20 GB of memory, whereas the DRM layer force storage requires only about 800 MB, and the reduced MLM-DRM model requires approximately 2.25 GB of memory. These results clearly demonstrate that the proposed MLM-DRM framework achieves substantial reductions in computational cost and memory requirements while maintaining high accuracy in reproducing the seismic response of the full-domain model, providing a robust numerical framework for the subsequent

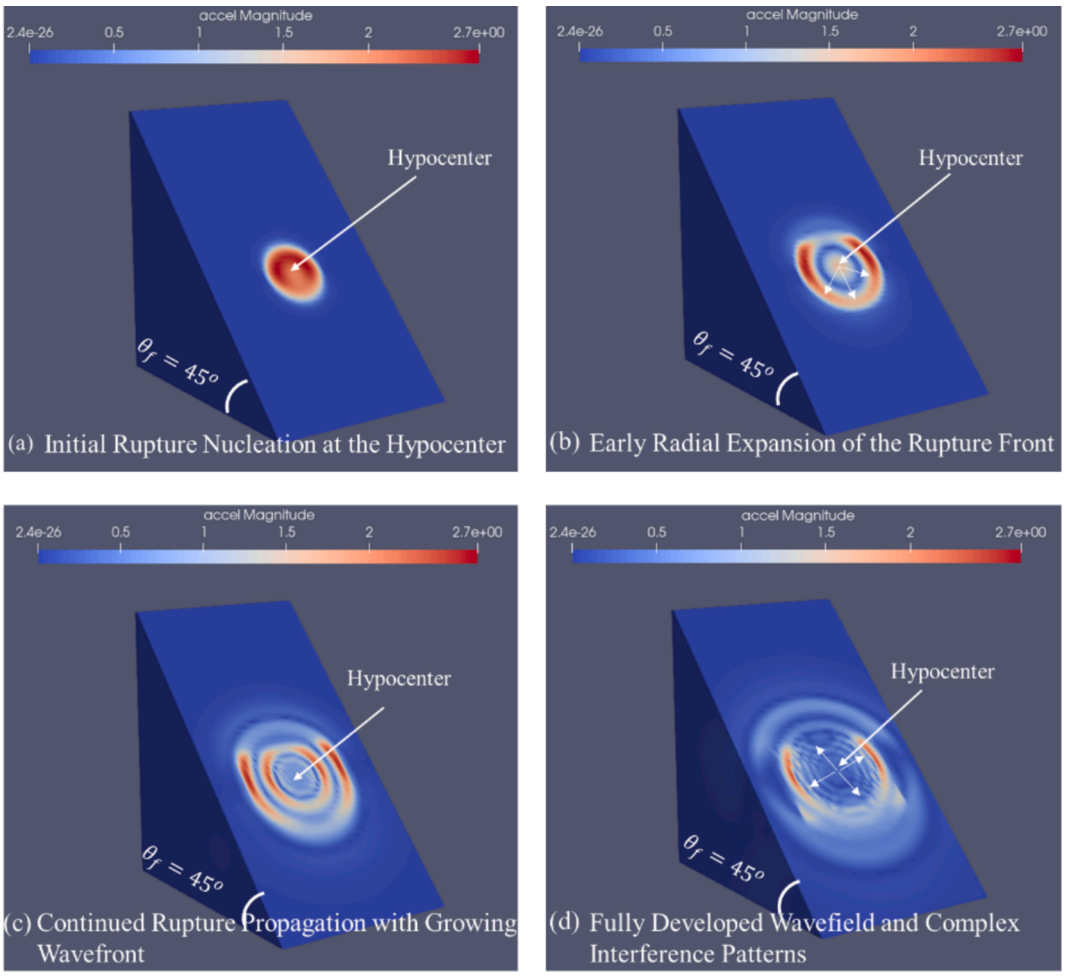


Fig. 18. Spatio-temporal evolution of the rupture and the resulting asynchronous ground motion for the fault inclined at $\theta_f = 45^o$ (a) Initial rupture, (b) Early radial expansion, (c) Growing wavefront, and (d) Fully developed wavefront.

parametric studies.

5. Parametric sensitivity analysis: Results and discussion

This section presents a systematic evaluation of the seismic performance of tunnels embedded in complex, inclined layered geologic media subjected to asynchronous fault rupture. The discussion begins with a numerical example to illustrate the interaction between fault-induced wave propagation and tunnel response in a three-dimensional setting. The analysis then focuses on the evolution and peak values of von Mises stress for different geological profiles and tunnel cross-sections, highlighting the role of asynchronous wave passage. Particular emphasis is placed on comparing tunnel responses under two fault inclinations (30° and 45°), examining both the temporal evolution of stresses and their spatial redistribution around the tunnel circumference. The influence of layer inclination is consistently assessed by considering increasing dip which amplifies stress asymmetry and alters critical stress locations. It is noted that the results provide insight into the coupled effects of fault inclination, inclined stratigraphy, and asynchronous ground motion on the seismic performance of tunnel.

5.1. Numerical example of tunnel in complex geologic media

The influence of layer inclination and tunnel geometry under realistic seismic loading is investigated systematically by performing parametric studies using the MLM-DRM. The subsurface is considered as a six-layer stratified media underlain by a competent bedrock layer, with shear wave velocities increasing with depth to represent realistic stiffness gradation. From top to bottom, the shear wave velocities are $V_{S1} = 383.5$ m/s, $V_{S2} = 607$ m/s, $V_{S3} = 836.7$ m/s, $V_{S4} = 932.5$ m/s, $V_{S5} = 1113.6$ m/s, and $V_{S6} = 1490.7$ m/s, corresponding to soft soil near the surface transitioning to stiff soil and rock at greater depths. This velocity profile enables realistic simulation of wave amplification, refraction, and mode conversion effects associated with layered ground conditions. Three tunnel cross-sections, namely, circular, horseshoe, and square are considered (see Fig. 10(a–c)). All tunnel sections are normalized to have the same excavation area, allowing direct comparison of their seismic performance while isolating the effect of geometric shape on stress distribution and wave-structure interaction.

To capture the role of inclined layers, the layered media is systematically rotated to form inclined stratigraphy with inclination angles $\theta_{inc} = 0°, 5°, 10°, 15°, 20°, 25°, 30°, 45°$, and 60°, as shown in Fig. 11(a–i). These configurations represent a wide spectrum of realistic subsurface conditions encountered in mountainous terrain, sedimentary basins, and fault-controlled geological environments. For each inclined geology, asynchronous seismic excitation is applied considering fault rupture inclinations of 30° and 45°, thereby incorporating wave-passage effects and non-uniform ground motion along the tunnel axis. The combined consideration of inclined layering and asynchronous fault rupture allows detailed assessment of how wave incidence angle, geological dip, and tunnel geometry jointly influence stress concentration, wave scattering, and amplification mechanisms. The resulting seismic response is evaluated primarily in terms of von Mises stress distribution (σ_v), enabling identification of critical sections and comparative performance of

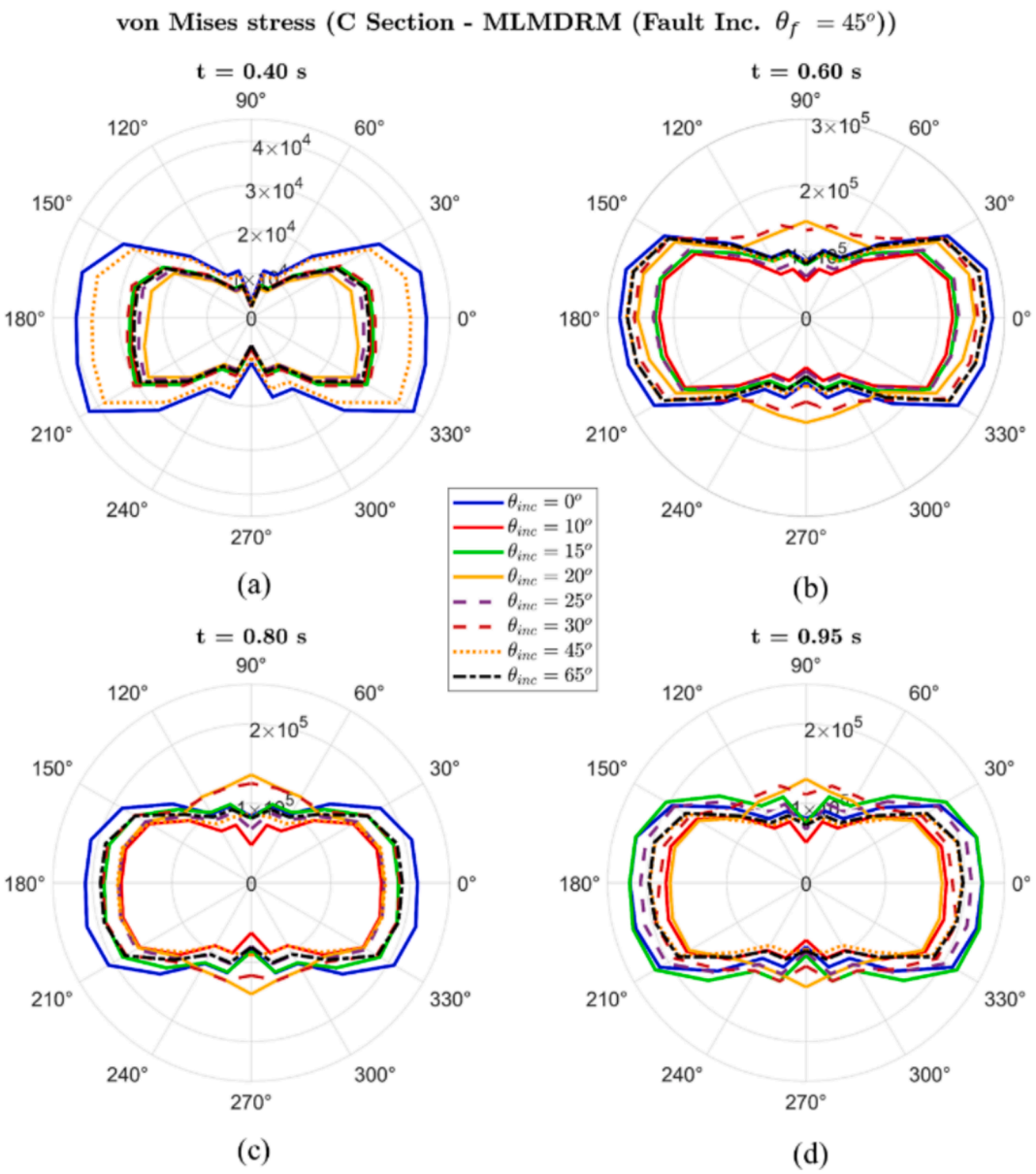


Fig. 19. Variation of von Mises stresses for different soil media around the circular section for fault inclined at $\theta_f = 45^o$: (a) t = 0.40 s, (b) t = 0.60 s, (c) t = 0.80 s, and (d) t = 0.95 s.

different tunnel shapes under increasingly complex geological and seismic conditions.

5.2. Peak von Mises stresses for different geologic profiles and fault inclinations

5.2.1. Fault inclination$\theta_f = 30^o$

5.2.1.1. Temporal evolution of von Mises stress around tunnel sections under asynchronous fault rupture ($\theta_f = 30^\circ$). Figs. 12–17 show the variation of von Mises stress around the tunnel circumference for circular (C), square (S), and horseshoe (H) sections subjected to asynchronous seismic excitation generated by fault inclined at $\theta_f = 30^\circ$, considering different inclined layered soil media. The results are shown at multiple time instants to capture both the arrival of strong seismic phases and the subsequent wave interaction and reverberation effects induced by the inclined stratigraphy.

For the circular tunnel section (Figs. 12 and 13), the stress distribution remains relatively symmetric at early times (t = 0.40–0.60 s), corresponding to the initial arrival of obliquely incident body waves. As time progresses (t = 0.80–0.95 s), the influence of inclined layering becomes evident, with increased stress amplitudes developing along preferential azimuthal directions. These directions align with the dominant wave-propagation path induced by asynchronous fault rupture. At later stages (t = 1.25–2.25 s), multiple wave reflections and surface wave interactions lead to a more complex stress pattern; however, the circular geometry continues to redistribute stresses efficiently, limiting peak amplification even for steeper soil layer inclinations. This confirms the inherent seismic robustness of circular tunnels under combined wave-passage and inclined geologic layer effects.

In contrast, the square tunnel section (Figs. 14 and 15) exhibits significantly higher stress concentrations from the early stages of shaking. At t = 0.40–0.60 s, pronounced stress peaks emerge at the corner regions, reflecting geometric discontinuities that act as stress raisers under dynamic loading. As the seismic response evolves (t = 0.80–0.95 s), inclined layered media amplify asymmetry in stress distribution, particularly for higher inclination angles, due to repeated wave refraction and constructive interference near sharp corners. At

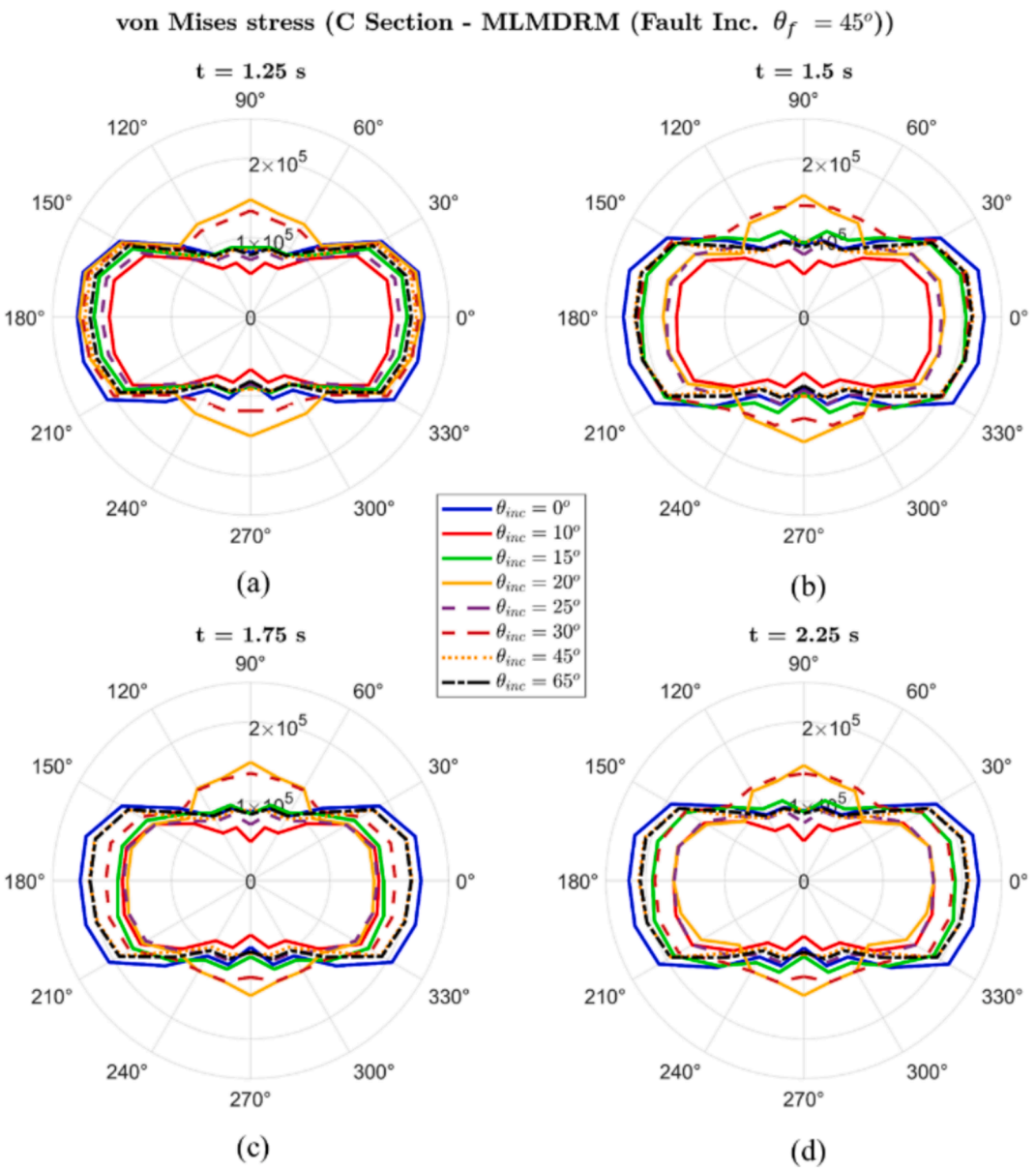


Fig. 20. Variation of von Mises stresses for different soil media around the circular section for fault inclined at $\theta_f = 45^o$: (a) t = 1.25 s, (b) t = 1.50 s, (c) t = 1.75 s, and (d) t = 2.25 s.

later times (t = 1.25–2.25 s), the combined effects of asynchronous wave arrival and geological inclination result in sustained high stress demand at the corners and mid-wall regions. These observations indicate that square tunnels are particularly vulnerable to prolonged dynamic loading under asynchronous excitation, especially in the inclined stratified ground.

The horseshoe tunnel section (Figs. 16 and 17) displays an intermediate but highly complex seismic response. At early times (t = 0.40–0.60 s), stress concentrations develop at the crown and haunch regions, driven by curvature transitions between the arch and sidewalls. As shaking intensifies (t = 0.80–0.95 s), the inclined layered media promotes uneven wave interaction along the lining, leading to asymmetric stress amplification. At later stages (t = 1.25–2.25 s), the horseshoe geometry exhibits persistent stress localization at the crown-sidewall junctions, exacerbated by asynchronous wave passage and surface wave trapping within the inclined layers. Compared to the circular section, the horseshoe tunnel experiences higher peak stresses, while still performing better than the square section due to partial geometric continuity.

Overall, Figs. 12–17 clearly demonstrate that asynchronous fault rupture and inclined layered geology jointly govern both the magnitude and spatial distribution of tunnel lining stresses. While circular tunnels show the most stable and uniform response across all time instants, non-circular sections particularly square tunnels are highly sensitive to wave-passage effects and layer inclinations. These results underscore the importance of three-dimensional asynchronous seismic modeling for realistic assessment of tunnel performance, as simplified synchronous or vertically propagating wave assumptions would fail to capture the observed temporal stress evolution and geometry-dependent amplification mechanisms.

5.2.1.2. Influence of inclined layers on tunnel stress response under asynchronous fault rupture. Figs. 12–17 illustrate the pronounced influence of layer inclinations on the circumferential distribution and temporal evolution of von Mises stresses around all tunnel sections subjected to asynchronous seismic excitation. For horizontally layered ground ($\theta_{inc} = 0°$), the stress distribution remains comparatively symmetric for all tunnel geometries, with peak stresses primarily governed by tunnel

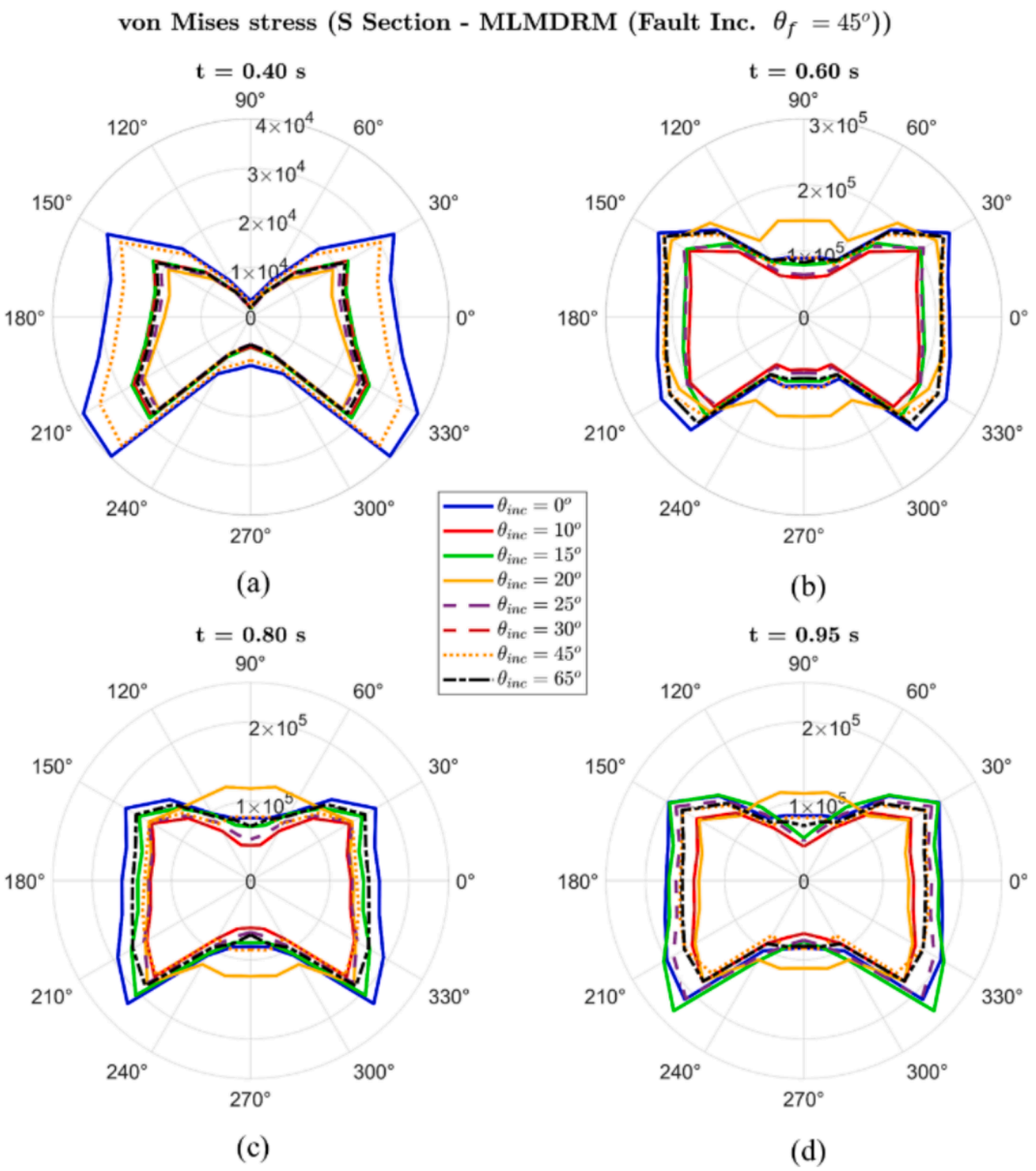


Fig. 21. Variation of von Mises stresses for different soil media around the square section for fault inclined at $\theta_f = 45^o$: (a) t = 0.40 s, (b) t = 0.60 s, (c) t = 0.80 s, and (d) t = 0.95 s.

shape and the arrival of dominant seismic phases. However, as the inclination angle increases, the layered media induces directional wave refraction, phase delay, and focusing, resulting in progressively asymmetric stress patterns around the tunnel periphery.

For the circular tunnel (see Figs. 12 and 13), the influence of layer inclinations on the circumferential von Mises stress distribution exhibits a non-monotonic trend with increasing layer inclination angles. At early times (t = 0.40–0.60 s), stress patterns remain relatively symmetric for gentle inclinations (θ_{inc} = 0°–10°), with a gradual reduction in peak stress magnitudes as θ_{inc} increases within this range. As the inclination increases further, the stress amplification becomes evident, reaching a maximum value around $\theta_{inc} = 20°$. At this inclination, the peak stresses are predominantly observed along the vertical axis (90° and 270°), indicating enhanced wave refraction and focusing effects due to inclined layering. Along the horizontal axis (0° and 180°), localized stress maxima are observed at $\theta_{inc} = 15°$, reflecting a transition in dominant wave-interaction mechanisms. Beyond θ_{inc} = 20°, the stress magnitudes reduce again, suggesting partial redistribution of seismic energy within steeper stratigraphy. However, for steeply inclined strata ($\theta_{inc} \geq 45°$) and at later times (t = 2.25 s), the peak stresses reappear along 0° and 180°, demonstrating the cumulative influence of asynchronous wave arrival, multiple reflections, and prolonged wave-layer interactions. These observations confirm that even for a geometrically optimal circular section, inclined geology combined with asynchronous excitation can significantly alter both the magnitude and angular location of stress concentrations.

In contrast to the circular tunnel, the square section (see Figs. 14 and 15) exhibits a much stronger sensitivity to layer inclination due to the presence of sharp corners and flat sidewalls. For low inclination angles (θ_{inc} = 0°–10°), stress concentrations are already evident at the corners, even during the early stages of shaking. As the layer inclination increases, these corner stresses intensify markedly, with peak von Mises stresses occurring earlier in time (t = 0.60–0.80 s) and persisting through the later stages (t = 1.25–2.25 s) of shaking. At moderate inclinations (θ_{inc} = 15°–25°), the stress amplification becomes severe, particularly along the diagonals of the square section, indicating strong wave focusing and trapping effects. These results demonstrate that square tunnels are highly vulnerable to slope-induced wave-passage

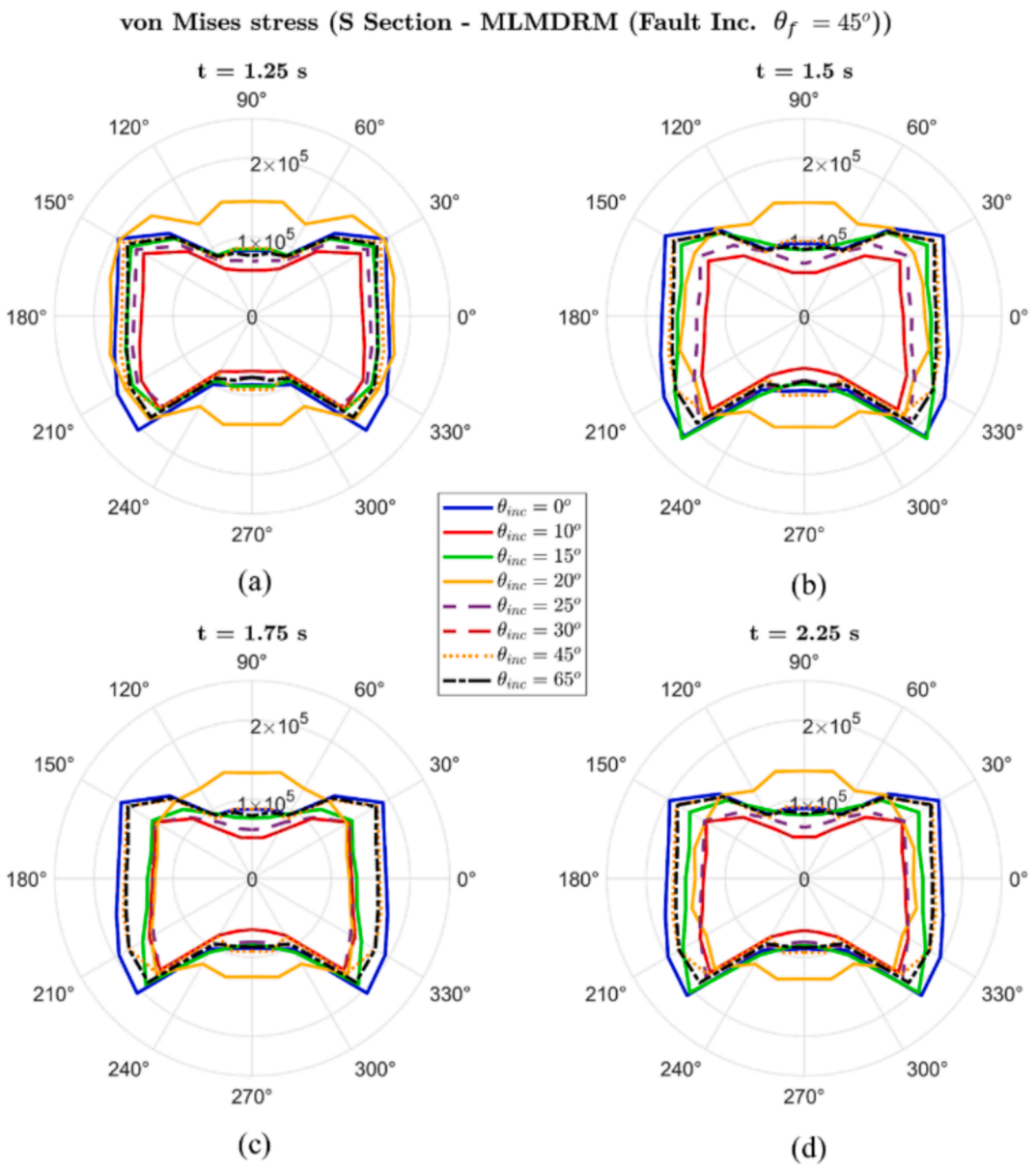


Fig. 22. Variation of von Mises stresses for different soil media around the square section for fault inclined at $\theta_f = 45^o$: (a) t = 1.25 s, (b) t = 1.50 s, (c) t = 1.75 s, and (d) t = 2.25 s.

effects under asynchronous seismic excitation, with geometric discontinuities exacerbating stress concentration and reducing seismic robustness.

The horseshoe tunnel (Figs. 16 and 17) exhibits an intermediate response between the circular and square sections. For small layer inclinations ($\theta_{inc} \leq 10^\circ$), the stress distribution remains relatively uniform, with moderate concentrations near the crown-haunch transition zones. As the inclination increases, stress amplification becomes increasingly asymmetric, particularly at the crown and upper sidewall regions, reflecting the combined influence of inclined layering and obliquely incident seismic waves. At $\theta_{inc} = 15^\circ$–30°, elevated stresses are observed near the arch-wall junctions during the strong motion phase (t = 0.60–0.95 s), while for steeper inclinations ($\theta_{inc} \geq 45^\circ$), the peak stresses persist into the later time (t = 1.25–2.25 s). This behavior highlights the enhanced surface-wave interaction and prolonged dynamic loading near the tunnel crown. Although the horseshoe geometry performs better than the square section by partially smoothing stress transitions, it remains significantly more sensitive to layer inclination effects than the circular tunnel under asynchronous fault rupture.

Based on the results, it can be demonstrated that the layer inclination acts as a critical amplifier of asynchronous wave-passage effects, with its influence becoming increasingly dominant as the layer inclination increases. The combined effects of inclined layering and asynchronous fault rupture lead to non-uniform stress amplification, azimuthal migration of peak stresses, and prolonged dynamic demand, none of which can be captured using the conventional synchronous or vertically propagating wave assumptions. These findings emphasize that the layer inclination must be explicitly considered in three-dimensional seismic response analysis and design of tunnels and underground structures particularly for non-circular sections constructed in faulted or mountainous terrains.

5.2.2. *Fault inclination* $\theta_f = 45^o$

5.2.2.1. Spatio-temporal rupture evolution and asynchronous ground motion. Fig. 18 shows the spatio-temporal evolution of rupture propagation and the resulting asynchronous ground motions for a fault inclined at $\theta_f = 45^\circ$. Unlike the $\theta_f = 30^\circ$ case (see Fig. 6(a)), the steeper

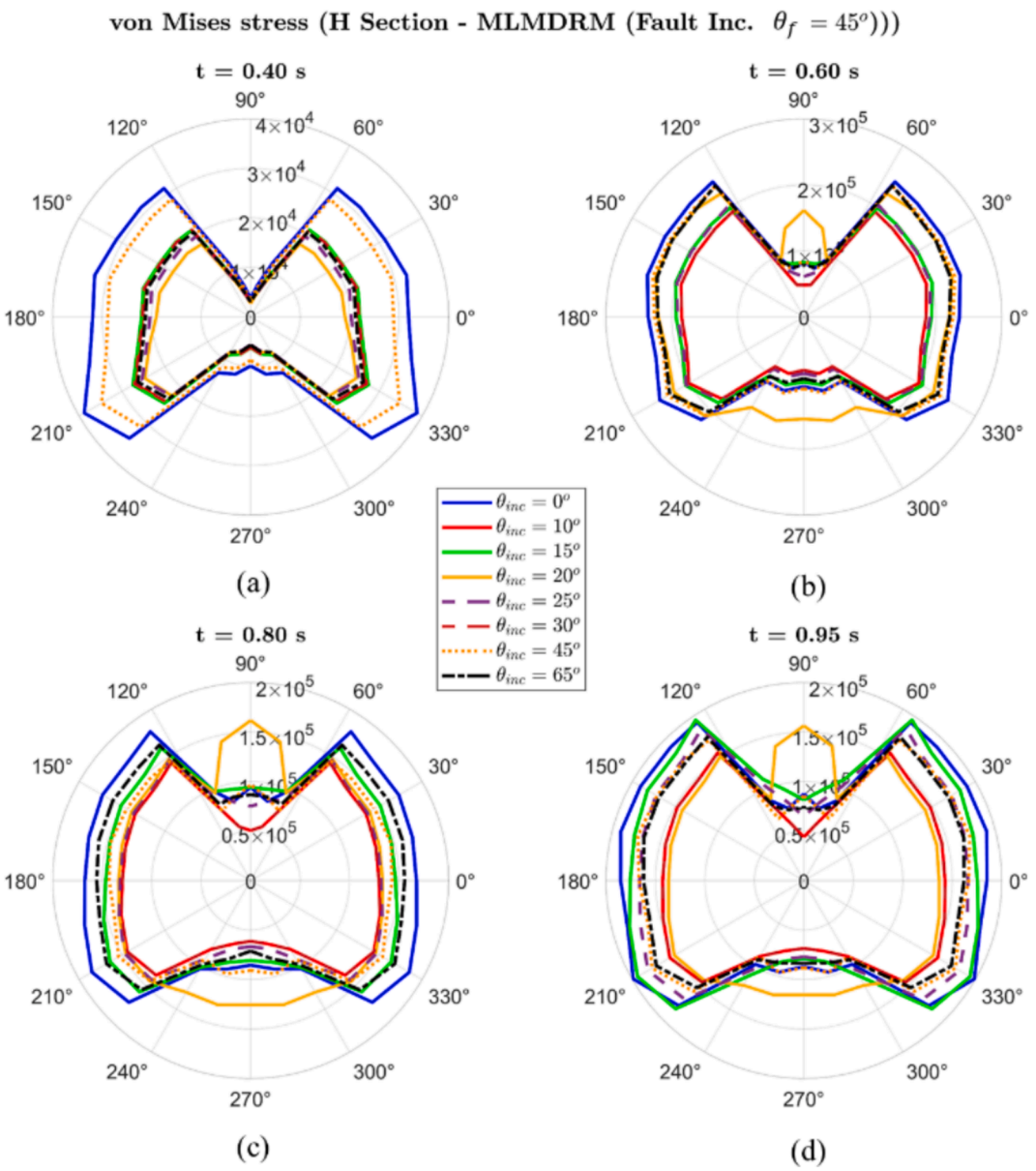


Fig. 23. Variation of von Mises stresses for different soil media around the horseshoe section for fault inclined at $\theta_f = 45^o$: (a) t = 0.40 s, (b) t = 0.60 s, (c) t = 0.80 s, and (d) t = 0.95 s.

fault geometry produces a more pronounced directional rupture growth, leading to strong spatial gradients in wave arrival times and amplitudes. The rupture initiates locally (Fig. 18(a)), followed by asymmetric radial expansion (Fig. 18(b)), where wavefronts propagate faster along the up-dip direction. As rupture progresses (Fig. 18(c)), the inclined geometry promotes oblique incidence of seismic waves onto the tunnel domain, generating significant wave-passage effects. At later stages (Fig. 18(d)), the fully developed wavefield exhibits clear time lags and phase differences across the domain, confirming the inherently asynchronous nature of the input motion. This behavior forms the governing excitation mechanism responsible for the complex stress patterns observed in the subsequent tunnel response.

5.2.2.2. Response of circular tunnel under asynchronous rupture. Figs. 19 and 20 illustrate the temporal evolution of von Mises stresses around the circular tunnel section at early (t = 0.40–0.95 s) and later (t = 1.25–2.25 s) stages of the ground motion, respectively. At early stages (Fig. 19(a-d)), stress concentrations develop primarily along the horizontal springlines (0° and 180°). The response is initially governed by the case of horizontal layering (layer inclination = 0°), while the maximum stress amplification is observed for a layer inclination of 20°, occurring predominantly along the vertical axis (90° and 270°). This behavior reflects the dominant direction of wave incidence and shear deformation induced by obliquely propagating seismic waves. Compared with the fault inclination $\theta_f = 30°$ case, stress amplitudes are noticeably higher, indicating a stronger dynamic interaction between the steeper rupture inclination and the tunnel lining.

As time progresses (Fig. 20(a–d)), the stress distribution becomes more circumferentially uniform; however, clear asymmetry persists, particularly for higher inclinations of the layers. At later stages, the response remains governed by layer inclination angle of 20°, with peak stresses concentrated along 90° and 270° azimuth, while secondary maxima are observed for layer inclination = 0° along 0° and 180° azimuth. Increasing the layer inclination amplifies the impedance contrasts around the tunnel periphery, leading to localized stress magnification on the up-dip side. These results demonstrate that even for geometrically symmetric circular tunnels, the combined effects of asynchronous fault rupture and inclined stratigraphy generate persistent non-uniform stress

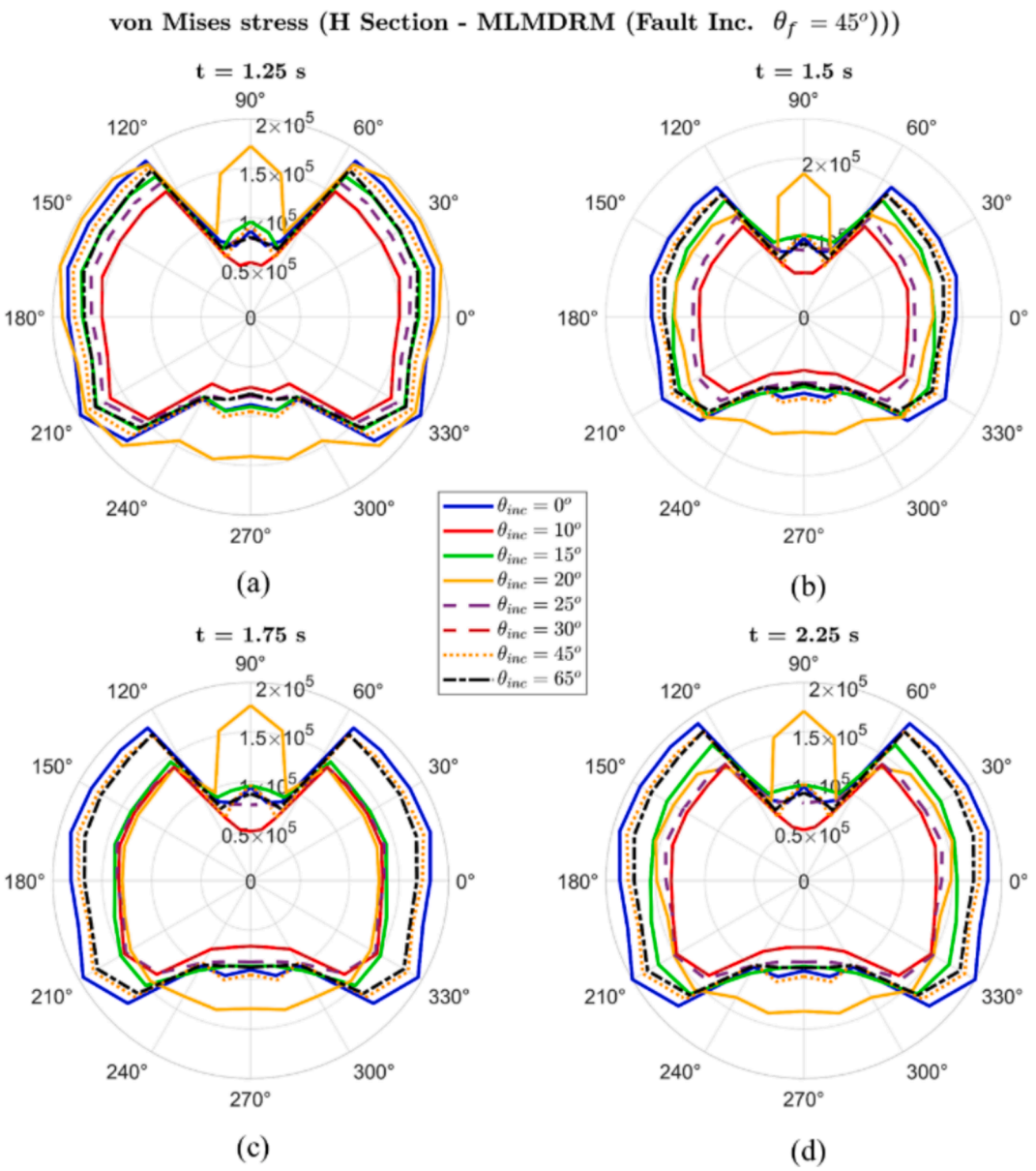


Fig. 24. Variation of von Mises stresses for different soil media around the horseshoe section for fault inclined at $\theta_f = 45^o$: (a) t = 1.25 s, (b) t = 1.50 s, (c) t = 1.75 s, and (d) t = 2.25 s.

Table 1
Summary of peak demand ratios and critical stress locations for different tunnel shapes under asynchronous fault rupture.

Tunnel shape	Fault inclination	Inlination of layer	Peak demand ratio(s)*	Critical locations	Temporal occurrence	Key observations
Circular	30°	Moderate increase with slope	1.00 (baseline)	Springline (0°-180°), minor crown involvement	Early (0.6–0.95 s after seismic excitation), stabilizes later	Uniform stress redistribution, least sensitivity to slope
Circular	45°	Strong amplification with slope	1.15–1.30	Shifted toward up-dip springline and crown	Early to mid (0.6–1.25 s)	Asymmetry in stress distribution due to rupture directivity
Square	30°	Significant amplification with slope	1.40–1.65	Corners (primary), mid-wall (secondary)	Persistent (0.6–2.25 s)	Strong stress concentration due to geometric discontinuity
Square	45°	Severe amplification with slope	1.70–2.10	Corners (dominant), alternating corners	Early and sustained (0.6–2.25 s)	Highest vulnerability under asynchronous loading
Horseshoe	30°	Moderate to high slope sensitivity	1.20–1.45	Crown-haunch junction, invert	Mid to late (0.8–2.25 s)	Mixed behavior due to partial curvature continuity
Horseshoe	45°	Strong slope-induced asymmetry	1.40–1.75	Crown (dominant), haunch zones	Mid to late (0.8–2.25 s)	Arch region highly affected by wave focusing

* Peak demand ratio = von Mises stress / von Mises stress evaluated with respect to circular tunnel under 30° fault inclination.

patterns.

5.2.2.3. Response of square tunnel and corner amplification. Figs. 21 and 22 depict the von Mises stress evolution for the square tunnel section. At early times (Fig. 21(a–d)), pronounced stress concentration occurs at the corners, where geometric discontinuities interact with obliquely incident shear waves. The effect is significantly stronger than in the circular section, with peak stresses aligning with the direction of rupture-controlled wave passage.

At later times (Fig. 22(a–d)), stress redistribution occurs as multiple reflected and transmitted wave components interact within the layered media. However, the corners remain critical zones of stress accumulation, particularly under higher layer inclinations. The combined effect of asynchronous loading and inclined geology leads to alternating stress dominance between adjacent corners, highlighting the sensitivity of non-circular sections to spatially varying seismic input motion.

5.2.2.4. Response of horseshoe tunnel and arch-invert interaction. Figs. 23 and 24 show the responses of horseshoe tunnel section. At early stages (Fig. 23(a–d)), the stress localization is observed near the arch shoulders and invert junctions where the curvature changes abruptly. The inclined rupture induces asymmetric loading, causing higher stresses on the side facing the advancing rupture front.

At later times (Fig. 24(a–d)), stress patterns evolve into a broader distribution along the arch, with secondary concentration at the invert. Compared to the square section, the horseshoe geometry exhibits improved stress redistribution; however, it remains more vulnerable than the circular section due to geometric non-uniformity. Increasing layer inclination further enhances stress asymmetry, particularly in the arch region, emphasizing the role of layered inclination in modifying the wave-structure interaction.

5.2.2.5. Influence of inclination of geologic media on tunnel response. From Figs. 19–24, the influence of inclined layers on the seismic response is clearly evident for all the three tunnel geometries considered in the study. Increasing the inclination leads to (i) enhanced wave refraction and reflection at stratified interfaces, (ii) increased phase lag between different portions of the tunnel lining due to asynchronous wave arrival, and (iii) systematic amplification of von Mises stress on the up-dip side of the tunnel. Notably, layer inclinations of 0°, 15°, and 20° emerge as critical configurations, at which distinct shifts in stress localization and dominant angular positions are observed. These effects are significantly more pronounced for a fault inclination of $\theta_f = 45°$ compared to $\theta_f = 30°$, confirming that steeper fault geometries intensify asynchronous wave-passage phenomena and exacerbate stress non-uniformity around tunnel linings.

The primary objective of the study is to investigate the influence of fault inclination (30° and 45°), inclined layered geology, and tunnel cross-sectional shape on seismic response using a consistent asynchronous input motion. Therefore, the rupture velocity and rise time are kept constant to isolate the effects of these governing parameters. It is important to note that variations in rupture velocity and rise time would modify the temporal coherence, wavefront propagation speed, and frequency content of the generated seismic waves, thereby influencing the degree of asynchronicity in ground motion. However, based on the established seismic wave propagation theory and prior studies on asynchronous excitation (Veeraraghavan et al., 2020), the trends observed in this study – such as increased stress concentration with geological inclination, higher demand under 45° fault inclination, and sensitivity of non-circular tunnel shapes – are governed primarily by wave-passage effects and geometric discontinuities, and are therefore expected to remain consistent.

5.2.3. Critical locations of tunnels and comparison of peak demands

A comparison of tunnel performance under asynchronous seismic excitation is carried out based on the stress evolution results presented in Figs. 12–24 for fault inclinations of 30° and 45°. The comparison (see Table 1) highlights consistent trends in peak demand and critical stresses occur at different locations across different tunnel geometries and geological conditions. It is observed that circular tunnels exhibit the most stable and uniform stress distribution, with peak stresses generally localized near the springline and showing a minimal sensitivity to increasing layer inclinations. In contrast, square tunnels demonstrate the highest stress amplification, with persistent concentration at corner regions due to geometric discontinuities, further intensified under higher fault inclination (45°) and steeper layered media. Horseshoe tunnels show intermediate behavior, with stress localization primarily occurring at the crown-haunch and invert junctions, and increasing asymmetry with slope angles. Across all tunnel types, the 45° fault inclination consistently produces higher peak demands and stronger spatial variability due to enhanced rupture directivity and wave-passage effects. Additionally, the increase geological inclination systematically shifts critical stress locations toward the up-dip side of the tunnel and prolongs the duration of peak stress demand. These observations confirm that both tunnel geometry and realistic asynchronous seismic input play a crucial role in governing the tunnel response and must be explicitly considered in the earthquake resistant design of tunnels.

6. Summary and conclusions

A comprehensive three-dimensional seismic response assessment of underground tunnels with circular, square, and horseshoe cross-sections embedded in geologically complex, multi-layered soil media is presented in the study using the developed MLM-DRM framework. The proposed framework extends the classical DRM by explicitly incorporating stratified soil layering, inclined geological interfaces, Rayleigh damping, and asynchronous fault-rupture-induced seismic input. These enhancements have enabled realistic simulation of wave refraction, scattering, attenuation, and wave-passage effects that are characteristic of actual earthquake scenarios. A key highlight of the present study is the explicit modeling of asynchronous fault rupture and its three-dimensional wave-propagation effects on the seismic performance of tunnel boundary. The results clearly demonstrate that asynchronous wave arrival and obliquely incident seismic waves significantly influence the temporal evolution and spatial distribution of stresses around the tunnel circumference. Compared with the idealized synchronous or vertically propagating wave assumptions, asynchronous excitations generate pronounced non-uniform stress patterns along the tunnel perimeter, highlighting the critical importance of incorporating finite-fault rupture mechanisms and realistic source modeling in seismic response analysis and design of underground structures.

The accuracy and computational efficiency of the MLM-DRM framework are verified through detailed comparisons with full-domain three-dimensional simulations. Despite a substantial reduction in computational cost, the reduced-domain MLM-DRM model successfully reproduces the spatio-temporal stress evolution induced by asynchronous fault rupture. This demonstrates that the proposed approach reliably captures complex wave-structure interaction phenomena while remaining suitable for large-scale parametric investigations relevant to engineering applications.

The influence of inclination of the layered geologic media is identified as a governing factor in the seismic performance assessment of tunnels. Increasing the inclination of the layered strata enhances wave refraction and impedance contrast at layer interfaces, leading to asymmetric stress distributions and localized stress amplification around the tunnel boundary. Critical inclination angles of the geologic layers, particularly around 0°, 15°, and 20°, consistently exhibit peak stress concentrations due to constructive wave interference and phase lag effects. These phenomena become more pronounced under steeper layer inclinations and higher fault dip angles ($\theta_f = 45°$), demonstrating the strong coupling between fault geometry and inclined stratigraphy in

controlling the seismic demand on tunnels and underground structures.

Tunnel cross-sectional geometry plays a decisive role in stress redistribution under complex seismic loading. Circular tunnel sections exhibit the most uniform and stable von Mises stress response across all layer inclinations and fault scenarios, confirming their superior seismic performance. In contrast, square and horseshoe tunnels develop elevated stress concentrations at corners, arch shoulders, and wall-invert transition zones, making them more sensitive to asynchronous excitation and inclined layering. These findings indicate that non-circular tunnel geometries are particularly vulnerable in faulted and dipping geological environments and hence they require careful consideration in the seismic analysis and design.

Based on the outcomes of this study, it is recommended that the seismic analysis and design of tunnels in faulted and layered geologic media must explicitly account for asynchronous ground motion, layer inclination, and realistic fault-rupture mechanisms. It is noted that the circular tunnel sections are preferable in regions characterized by steeply inclined stratigraphy or active faulting, whereas non-circular sections require targeted reinforcement at critical stress concentration zones. It is opined that the future research study can be extended to include nonlinear soil behavior, soil-structure interface effects, and spatial variability of material properties and fault rupture mechanism, thereby strengthening the reliability and resilience of underground infrastructure facing complex engineering geological challenges.

CRediT authorship contribution statement

Bhavesh Banjare: Writing – original draft, Visualization, Validation, Software, Methodology, Investigation, Formal analysis, Data curation, Conceptualization. **Gauri Ranjan Krishna Chand Avatar:** Writing – review & editing, Visualization, Methodology, Conceptualization. **Goudappa Ramanagouda Dodagoudar:** Writing – review & editing, Visualization, Supervision, Resources, Methodology.

Declaration of competing interest

The authors declare that they have no known competing financial interests or personal relationships that could have appeared to influence the work reported in this paper.

Acknowledgments

Authors sincerely acknowledge the support provided by the MoE (Ministry of Education, Govt. of India) and computational geomechanics laboratory of Indian Institute of Technology Madras, Chennai, India.

Data availability

Data will be made available on request.

References

Ahrabi, B.R., Mavriplis, D.J., 2020. An implicit block ILU smoother for preconditioning of Newton–Krylov solvers with application in high-order stabilized finite-element methods. Comput. Methods Appl. Mech. Eng. 358, 112637. https://doi.org/10.1016/J.CMA.2019.112637.

Aki, K., Richards, P.G., 2002. *Quantitative seismology*. University Science Books, Mill Valley, California.

Alterman, Z., Karal, F.C., 1968. Propagation of elastic waves in layered media by finite difference methods. Bull. Seismol. Soc. Am. 58 (1), 367–398. https://doi.org/10.1785/BSSA0580010367.

Anastasopoulos, I., Gerolymos, N., Drosos, V., Georgarakos, T., Kourkoulis, R., Gazetas, G., 2007. Behaviour of deep immersed tunnel under combined normal fault rupture deformation and subsequent seismic shaking. *Bulletin of Earthquake Engineering 2007 6:2*, *6*(2), 213–239. https://doi.org/10.1007/S10518-007-9055-0.

Aydan, Malistani, N., Ulusay, R., Kumsar, H., 2024. The damage and response of some underground structures by the 2023 February 6 Great Turkish Earthquakes and some considerations. Eng. Geol., *336*, 107549. https://doi.org/10.1016/J.ENGGEO.2024.107549.

Banjare, B., Avatar, G.R.K.C., 2024. Stochastic assessment of 3-D tunnels in near-fault ground motion using modified domain reduction method. Int. J. Numer. Anal. Meth. Geomech. 48 (9), 2259–2284. https://doi.org/10.1002/NAG.3733.

Banjare, B., Avatar, G.R.K.C., Dodagoudar, G.R., 2025. Three-dimensional seismic response analysis of tunnels in layered media using modified domain reduction method. Int. J. Numer. Anal. Meth. Geomech. 49 (13), 3027–3047. https://doi.org/10.1002/NAG.70006.

Bielak, J., Christiano, P., 1984. On the effective seismic input for non-linear soil-structure interaction systems. Earthq. Eng. Struct. Dyn. 12 (1), 107–119. https://doi.org/10.1002/EQE.4290120108.

Bielak, J., Loukakis, K., Hisada, Y., Yoshimura, C., 2003. Domain reduction method for three-dimensional earthquake modeling in localized regions, part I: Theory. Bull. Seismol. Soc. Am. 93 (2), 817–824. https://doi.org/10.1785/0120010251.

Boore, D.M., 1972. A note on the effect of simple topography on seismic SH waves. Bull. Seismol. Soc. Am. 62 (1), 275–284. https://doi.org/10.1785/BSSA0620010275.

Chen, G., Jin, D., Mao, J., Gao, H., Wang, Z., Jing, L., Li, Y., Li, X., 2014. Seismic damage and behavior analysis of earth dams during the 2008 Wenchuan earthquake, China. Eng. Geol. 180, 99–129. https://doi.org/10.1016/J.ENGGEO.2014.06.001.

Chen, P., Geng, P., Chen, J., Gu, W., 2023. The seismic damage mechanism of Daliang tunnel by fault dislocation during the 2022 Menyuan Ms6.9 earthquake based on unidirectional velocity pulse input. Eng. Fail. Anal. 145, 107047. https://doi.org/10.1016/J.ENGFAILANAL.2023.107047.

Coleman, J., Slaughter, A., Veeraraghavan, S., Bolisetti, C., Numanoglu, O. A., Spears, R., Hoffman, W., Hurt, E., 2017. *MASTODON Theory Manual*. https://doi.org/10.2172/1376857.

Corigliano, M., Scandella, L., Lai, C.G., Paolucci, R., 2011. Seismic analysis of deep tunnels in near fault conditions: a case study in Southern Italy. Bull. Earthq. Eng. 9 (4), 975–995. https://doi.org/10.1007/S10518-011-9249-3/METRICS.

Cui, X., Liu, Y., Du, X., Xiao, H., Xu, H., Du, Y., 2025. Effect of fault dislocation on the deformation and damage behavior of ballastless track structures in tunnels. Transp. Geotech. 52, 101561. https://doi.org/10.1016/J.TRGEO.2025.101561.

Fabozzi, S., Bilotta, E., Yu, H., Yuan, Y., 2018. Effects of the asynchronism of ground motion on the longitudinal behaviour of a circular tunnel. Tunn. Undergr. Space Technol. 82, 529–541. https://doi.org/10.1016/J.TUST.2018.09.005.

Fang, H., Lai, Z., Qu, C., 2024. Investigation of seismic amplification on soil–structure interaction problems based on a 3D DRM-RFEM framework. ASCE-ASME J. Risk Uncertain. Eng, Syst. Part A: Civ. Eng. 10 (1). https://doi.org/10.1061/ajrua6.rueng-1181.

Gurung, N., Iwao, Y., 1998. Observations of deformation and engineering geology in the Lam Ta Khong tunnel, Thailand. Eng. Geol. 51 (1), 55–63. https://doi.org/10.1016/S0013-7952(98)00031-3.

Hatzigeorgiou George D., G. D., Beskos, D. E., 2010. Soil–structure interaction effects on seismic inelastic analysis of 3-D tunnels. *Soil Dynamics and Earthquake Engineering*, *30* (9), 851–861. https://doi.org/10.1016/J.SOILDYN.2010.03.010.

Heider, Y., Markert, B., Ehlers, W., 2011. Dynamic wave propagation in infinite saturated porous media half spaces. *Computational Mechanics 2011 49:3*, *49*(3), 319–336. https://doi.org/10.1007/S00466-011-0647-9.

Huang, H.W., Xiao, L., Zhang, D.M., Zhang, J., 2017a. Influence of spatial variability of soil Young's modulus on tunnel convergence in soft soils. Eng. Geol. 228, 357–370. https://doi.org/10.1016/J.ENGGEO.2017.09.011.

Huang, J., Zhao, M., Du, X., 2017b. Non-linear seismic responses of tunnels within normal fault ground under obliquely incident P waves. Tunn. Undergr. Space Technol. 61, 26–39. https://doi.org/10.1016/J.TUST.2016.09.006.

Huang, S., Xin, C., Song, D., Feng, W., Liu, X., Wang, E., Xu, T., Xiong, X., 2024. Resilience assessment of the seismic damage mechanism of the Daliang high-speed railway tunnel in the 2022 Menyuan earthquake (M_w 6.7) in China. Transp. Geotech. 49, 101417. https://doi.org/10.1016/J.TRGEO.2024.101417.

Ihlenburg, F., Babuška, I., 1995. Finite element solution of the Helmholtz equation with high wave number Part I: the h-version of the FEM. Comput. Math. Appl. 30 (9), 9–37. https://doi.org/10.1016/0898-1221(95)00144-N.

Kontoe, S., Zdravkovic, L., Potts, D., 2008. The domain reduction method for dynamic coupled consolidation problems in geotechnical engineering. Int. J. Numer. Anal. Meth. Geomech. 32 (6), 659–680. https://doi.org/10.1002/NAG.641.

Kontoe, S., Zdravkovic, L., Potts, D.M., 2009. An assessment of the domain reduction method as an advanced boundary condition and some pitfalls in the use of conventional absorbing boundaries. Int. J. Numer. Anal. Meth. Geomech. 33 (3). https://doi.org/10.1002/nag.713.

Lee, V.W., Cao, H., 1989. Diffraction of SV Waves by Circular Canyons of Various Depths. J. Eng. Mech. 115 (9), 2035–2056. https://doi.org/10.1061/(ASCE)0733-9399(1989)115:9(2035).

Lee, V.W., Karl, J., 1992. Diffraction of SV waves by underground, circular, cylindrical cavities. Soil Dyn. Earthq. Eng. 11 (8), 445–456. https://doi.org/10.1016/0267-7261(92)90008-2.

Levander, A.R., 2012. Fourth-order finite-difference P-SV seismograms. Geophysics. doi 10 (1190/1), 1442422.

Li, P., Song, E.X., 2015. Three-dimensional numerical analysis for the longitudinal seismic response of tunnels under an asynchronous wave input. Comput. Geotech. 63, 229–243. https://doi.org/10.1016/j.compgeo.2014.10.003.

Lin, C.H., Lee, V.W., Todorovska, M.I., Trifunac, M.D., 2010. Zero-stress, cylindrical wave functions around a circular underground tunnel in a flat, elastic half-space: Incident P-waves. Soil Dyn. Earthq. Eng. 30 (10), 879–894. https://doi.org/10.1016/J.SOILDYN.2010.01.010.

Lysmer, J., Kuhlemeyer, R.L., 1969. Finite Dynamic Model for Infinite Media. J .Eng. Mech. Div. 95 (4), 859–877. https://doi.org/10.1061/JMCEA3.0001144.

Moczo, P., Bystrický, E., Kristek, J., Carcione, J.M., Bouchon, M., 1997. Hybrid modeling of P-SV seismic motion at inhomogeneous viscoelastic topographic structures. Bull. Seismol. Soc. Am. 87 (5), 1305–1323. https://doi.org/10.1785/BSSA0870051305.

Newmark, N.M., 1959. A Method of Computation for Structural Dynamics. J .Eng. Mech. Div. 85 (3), 67–94. https://doi.org/10.1061/JMCEA3.0000098.

Opršal, I., Zahradník, J., 2012. Elastic finite-difference method for irregular grids. Https://Doi.Org/10.1190/1.1444520 64 (1), 240–250. https://doi.org/10.1190/1.1444520.

Paolucci, R., 2002. Amplification of earthquake ground motion by steep topographic irregularities. Earthq. Eng. Struct. Dyn. 31 (10), 1831–1853. https://doi.org/10.1002/EQE.192.

Sánchez-Sesma, F.J., 1990. Elementary solutions for response of a wedge-shaped medium to incident SH and SV waves. Bull. Seismol. Soc. Am. 80 (3), 737–742. https://doi.org/10.1785/BSSA0800030737.

Sánchez-Sesma, F.J., Herrera, I., Avilés, J., 1982. A boundary method for elastic wave diffraction: Application to scattering of SH waves by surface irregularities. Bull. Seismol. Soc. Am. 72 (2), 473–490. https://doi.org/10.1785/BSSA0720020473.

Schauer, M., Langer, S., Roman, J. E., Quintana-Ortí, E. S., 2011. Large scale simulation of wave propagation in soils interacting with structures using fem and SBFEM. *19*(1), 75–93. https://doi.org/10.1142/S0218396X11004316.

Semblat, J.F., Kham, M., Parara, E., Bard, P.Y., Pitilakis, K., Makra, K., Raptakis, D., 2005. Seismic wave amplification: Basin geometry vs soil layering. Soil Dyn. Earthq. Eng. 25 (7–10), 529–538. https://doi.org/10.1016/J.SOILDYN.2004.11.003.

Seo, C.G., Yun, C.B., Kim, J.M., 2007. Three-dimensional frequency-dependent infinite elements for soil–structure interaction. Eng. Struct. 29 (11), 3106–3120. https://doi.org/10.1016/J.ENGSTRUCT.2007.02.006.

Sharma, S., Judd, W.R., 1991. Underground opening damage from earthquakes. Eng. Geol. 30 (3–4), 263–276. https://doi.org/10.1016/0013-7952(91)90063-Q.

Shen, Y., Gao, B., Yang, X., Tao, S., 2014. Seismic damage mechanism and dynamic deformation characteristic analysis of mountain tunnel after Wenchuan earthquake. Eng. Geol. 180, 85–98. https://doi.org/10.1016/J.ENGGEO.2014.07.017.

Sills, L.B., 1978. Scattering of horizontally-polarized shear waves by surface irregularities. Geophys. J. Int. 54 (2), 319–348. https://doi.org/10.1111/J.1365-246X.1978.TB04263.X.

Smerzini, C., Avilés, J., Paolucci, R., Sánchez-Sesma, F.J., 2009. Effect of underground cavities on surface earthquake ground motion under SH wave propagation. Earthq. Eng. Struct. Dyn. 38 (12), 1441–1460. https://doi.org/10.1002/EQE.912.

Tian, Y., Motalleb Qaytmas, A., Lu, D., Du, X., 2023. Stress path of the surrounding soil during tunnel excavation: an experimental study. Transp. Geotech. 38, 100917. https://doi.org/10.1016/J.TRGEO.2022.100917.

Trifunac, M.D., 1972. Scattering of plane SH waves by a semi-cylindrical canyon. Earthq. Eng. Struct. Dyn. 1 (3), 267–281. https://doi.org/10.1002/EQE.4290010307.

Veeraraghavan, S., Banjare, B., 2025. A modified domain reduction method for analysing the 3D seismic response of long tunnels. Tunn. Undergr. Space Technol. 159, 106461. https://doi.org/10.1016/J.TUST.2025.106461.

Veeraraghavan, S., Coleman, J.L., Bielak, J., 2020. Simulation of site and topographic effects on ground motion in Los Alamos, NM mesas. Geophys. J. Int. 220 (3), 1504–1520. https://doi.org/10.1093/GJI/GGZ448.

Vidale, J.E., Helmberger, D.V., 1988. Elastic finite-difference modeling of the 1971 San Fernando, California earthquake. Bull. Seismol. Soc. Am. 78 (1), 122–141. https://doi.org/10.1785/BSSA0780010122.

Wang, G., Shi, L., Wang, J., Zuo, P., Zhao, D., Sun, F., 2023. Experimental and numerical studies on the seismic response of adjacent horizontal parallel tunnels. Soil Dyn. Earthq. Eng. 172, 107992. https://doi.org/10.1016/J.SOILDYN.2023.107992.

Wang, W.L., Wang, T.T., Su, J.J., Lin, C.H., Seng, C.R., Huang, T.H., 2001. Assessment of damage in mountain tunnels due to the Taiwan Chi-Chi Earthquake. Tunn. Undergr. Space Technol. 16 (3), 133–150. https://doi.org/10.1016/S0886-7798(01)00047-5.

Wu, G., Zhao, H., Zhao, M., Zhu, Z., 2021. Stochastic analysis of dual tunnels in spatially random soil. Comput. Geotech. 129, 103861. https://doi.org/10.1016/J.COMPGEO.2020.103861.

Wu, S., Hu, X., Fu, W., Li, K., 2024. Evaluation of segmental lining response during shield tunnel construction based on field measurements and 3D FEM simulation. Transp. Geotech. 44, 101135. https://doi.org/10.1016/J.TRGEO.2023.101135.

Wuttke, F., Dineva, P., Schanz, T., 2011. Seismic wave propagation in laterally inhomogeneous geological region via a new hybrid approach. J. Sound Vib. 330 (4), 664–684. https://doi.org/10.1016/J.JSV.2010.08.042.

Yoshimura, C., Bielak, J., Hisada, Y., Fernández, A., 2003. Domain reduction method for three-dimensional earthquake modeling in localized regions, part ii: verification and applications. Bull. Seismol. Soc. Am. 93 (2), 825–841. https://doi.org/10.1785/0120010252.

Yu, H., Chen, J., Bobet, A., Yuan, Y., 2016. Damage observation and assessment of the Longxi tunnel during the Wenchuan earthquake. Tunn. Undergr. Space Technol. 54, 102–116. https://doi.org/10.1016/J.TUST.2016.02.008.

Yuan, Y., Fan, Z., Liu, F., Yang, Y., 2023. A DRM-SMM framework for wave propagation in layered saturated ground under inclined P1-SV waves. Comput. Geotech. 162, 105658. https://doi.org/10.1016/J.COMPGEO.2023.105658.

Zhang, X., Jiang, Y., Sugimoto, S., 2018. Seismic damage assessment of mountain tunnel: a case study on the Tawarayama tunnel due to the 2016 Kumamoto Earthquake. Tunn. Undergr. Space Technol. 71, 138–148. https://doi.org/10.1016/J.TUST.2017.07.019.

Zhong, Z., Wang, Z., Zhao, M., Du, X., 2020. Structural damage assessment of mountain tunnels in fault fracture zone subjected to multiple strike-slip fault movement. Tunn. Undergr. Space Technol. 104, 103527. https://doi.org/10.1016/J.TUST.2020.103527.

Zienkiewicz, O.C., Leung, K.H., Pastor, M., 1985. Simple model for transient soil loading in earthquake analysis. I. Basic model and its application. Int. J. Numer. Anal. Meth. Geomech. 9 (5), 453–476. https://doi.org/10.1002/NAG.1610090505.

Zou, Y., Liu, H., Jing, L., 2018. Response of long tunnel in layered half-space under asynchronous seismic shear-horizontal wave propagation. J. Eng. Mech. 144 (7), 04018050. https://doi.org/10.1061/(ASCE)EM.1943-7889.0001475/ASSET/.